NTNU

Norwegian University of
Science and Technology

Rhodium doped strontium titanate for photocatalytic hydrogen evolution with carbon quantum dots

Dani Espevik

Chemical Engineering and Biotechnology
Submission date: July 2018
Supervisor: Jia Yang, IKP
Co-supervisor: Magnus Rønning, IKP

Norwegian University of Science and Technology
Department of Chemical Engineering

Preface

This master thesis is written as part of the education program for chemical engineering at the Norwegian University of Science and Technology. The master thesis is a continuation from my specialization project, last semester and some of the content in this report is reproduced from that project.

When I chose this topic, it was not clear to me exactly what photocatalysis was, but for a long time, I have considered water splitting by different methods to be very interesting. If water splitting can be done in an energy efficient way, it has the potential to bring revolution to the energy challenges mankind are facing today.

I would like to thank my supervisor, Associate professor Jia Yang for accepting me into her photocatalysis group and for being available for help and guidance when needed. I would like to thank my Co-supervisor, Professor Magnus Rønning for valuable inputs and for help along the way. I would like to thank Ph.D. candidate Muhammad Zubair for his guidance and patience. He has also helped me keep up the mood in difficult times. I would also like to thank Dr. Qingjun Chen for preparing the carbon quantum dots and for his inputs along the way. In general, the photocatalysis group has been very helpful, and it is a privilege to have been a part of it.

Declaration of compliance

I hereby declare that this is an independent work according to the exam regulations of the Norwegian University of Science and Technology.

Trondheim, July 4, 2018

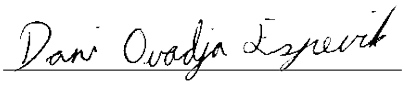

Dani Ovadja Espevik

And God said, let there be light and there was light

And God saw the light, that it was good and God divided the light from the darkness

Abstract

The worlds energy demands continue to increase, and the reserves of fossil fuels are limited. Therefore, the world is in need of finding different energy sources. Production of hydrogen by splitting water, using photocatalysis is a potential solution. Previous studies have shown that $SrTiO_3$ doped with Rh is active in the visible light area. The purpose of this study was to synthesize Rh doped $SrTiO_3$ and enhance the photocatalytic H_2 evolution with carbon quantum dots from a solution containing a sacrificial reagent. $SrTiO_3$ and Rh doped $SrTiO_3$ was synthesized from TiO_2, $SrCO_3$ and Rh_2O_3, using the solid state reaction method. The XRD specter showed the characteristic peaks for $SrTiO_3$ for all of the synthesized samples along with some impurity peaks. Previous studies have shown that the Sr/(Ti+Rh) ratio is important for achieving high activity from Rh doped $SrTiO_3$. The ratio was investigated using ICP-MS. UV-vis DRS measurements were used to obtain the absorbance spectra of the synthesized samples. The Rh doped $SrTiO_3$ sample prepared at 1100 °C (B8.Rh) is considered to be the most active of the synthesized samples and is exhibiting all the characteristics found in literature for Rh doped $SrTiO_3$ except for having a slightly larger band gap. However, the TiO_2 P25 from Sigma Aldrich with photodeposited Pt evolved H_2 at a much higher rate than the B8.Rh with photodeposited Pt. Carbon quantum dots was loaded on to the B8.Rh, but completely hampered the photocatalytic activity.

Sammendrag

Verdens energibehov fortsetter å øke og de fossile brennstoff lagrene er begrenset; verden trenger derfor å finne andre energi kilder. Å produsere hydrogen fra vann ved hjelp av fotokatalyse er en potensiell løsning. Tidligere studier har vist at $SrTiO_3$ dopet med Rh er aktiv i synlig lys. Hensikten med dette studiet var å fremstille Rh dopet strontium titanate og forbedre den fotokatalytiske hydrogenutviklingen ved hjelp av karbon kvanteprikker fra en løsning med en ofringsreagent. $SrTiO_3$ og Rh dopet $SrTiO_3$ ble fremstilt fra TiO_2, $SrCO_3$ og Rh_2O_3 ved bruk av en reaksjonsmetode for stoffer i fast fase. XRD analysene for alle de fremstilte prøvene viste alle de karakteristiske toppene for strontium titanate, sammen med noen små urenhetstopper. Tidligere studier har vist at Sr/(Ti+Rh) forholdet er viktig for å oppnå høy fotokatalytisk aktivitet fra Rh dopet $SrTiO_3$. Dette forholdet ble undersøkt med ICP-MS. UV-vis DRS målinger ble utført for å erverve absorbsjonsspektrene til de fremstilte prøvene. Rh dopet $SrTiO_3$, kalsinert ved 1100 °C (B8.Rh) er vurdert som den mest aktive av de fremstilte prøvene og viser alle de karakteristiske trekkene for Rh dopet strontium titanate med unntak av et litt større båndgap. Likevel produserte kommersiell TiO_2 P25 fra Sigma Aldrich mye mer hydrogen enn B8.Rh under aktivitetsmåling, når de begge var tilsatt fotodeponert Pt. B8.Rh ble impregnert med karbon kvanteprikker, men ingen fotokatalytisk aktivitet kunne spores i nærvær av karbon kvanteprikkene.

List of Symbols

n	is an integer which represents the order of reflection
λ	is the radiations wavelength
d	is the the length between two lattice planes
θ	is the angle the X-ray beam hits the reflecting lattice plane
$< L >$	is the particles measured dimension in the perpendicular direction of the reflecting plane
K	is constant
β	is the width of the peak
h	is Planck's constant
v	is the photons oscilation
E_0	is the optical absorption energy
η	factor for band gap transition
R	is reflectance
S	is scattering coeffisient
A	is absorption coeffisient
c	speed of light in vacuum
N_A	Avogadro's number

H	light intensity of the solar simulator
A_{QY}	is the geometric area of the sample
e	electron charge
λ_{QY} =	Average wavelength of broadband light source. Dependent on the band gap and light source.

Abbreviations

EJ	Exajoule
VB	Valence band
CB	Conduction band
CQDs	Carbon quantum dots
XRF	X-ray fluorescence
XRD	X-ray diffraction
BET	Brunauer, Emmett and Teller
PD	Photodeposited
ICP-MS	Inductive couplet plasma - Mass spectrometer
SSR	Solid state reaction
GC	Gas chromatography
UV-vis	UV-visible spectroscopy
$SrTiO_3$:Rh	denotes Rh doped $SrTiO_3$
MeOH	Methanol
wt%	weight percentage
I-R	Denotes photocatalyst Impregnated with Pt and then thermally reduced at 500 °C in H_2 flow, 100 $\frac{ml}{min}$

Contents

List of Figures

List of Tables

Chapter 1

Introduction

Slavery has been a part of nearly every society until the use of coal became widespread [1]. Slaves represented power, $\frac{Joules}{second}$ or Watt. Today we obtain that energy from fossil fuels. The fossil fuels allow the modern civilization to function without having to rely on people or domestic animal power. The fossil fuel has become the foundation of modern society. [1]

In 2008 the world used 514 exajoule (EJ) where 80% of that energy came from fossil fuels. The worlds energy demands are continuously increasing, and if the economic growth continues the growth of recent decades, the energy demand is projected to rise to 1000 EJ (EJ = 10^{18} J) or more by 2050. With over 80 % of the energy, coming from fossil fuels, fossil fuels are currently dominating the energy provision, but that cannot continue for more than a couple of decades. The reserves of easily extracted gas, oil and coal are all likely to have peaked by 2030. In addition to geological depletion, national resource politics will also determine the peak in output. There is also the CO_2 emissions from fossil fuels which are estimated to account for 74 % of all CO_2 emissions. Global levels of CO_2 in the atmosphere is now at 390 ppm (2011), and there are arguments from earth scientists that the current level should be reduced to 350 ppm[2], [3], mainly to preserve the Greenland ice cap. [4]

To solve the need for energy and to protect the environment from further pollution,

new energy sources are needed. The sun is an abundant energy source, and it is estimated that we generate 15000 GW today using the suns solar energy, excluding biomass combustion and solar heating. This is less than 0,05% of its technical potential. [4], [5]

Other energy sources can be considered such as nuclear fission. It is possible to supply 50 Terawatts of energy via nuclear fission. However, the number of nuclear power plants needed would be approximately a factor of 500 times the number of nuclear power plants ever built. This would result in depletion of earth's uranium supplies. [1]

Harvesting solar energy in an inexpensive, but efficient way appears to be the only solution to the worlds energy demands. Energy politics currently in vogue is looking to solve this by growing plants that subsequently can be turned into automobile fuel. The solar to fuel conversion efficiencies of plants are approximately 0.1%. Furthermore, the crops of plants are already used as either food or the organic matter that soil is made of which sustains agriculture. [1]

Hydrogen can be used in fuel cells and is also used in large amounts in the chemical industry, e.g., ammonia synthesis. At present most of the hydrogen is produced from fossil fuels by steam reforming of natural gas. In steam reforming, fossil fuels are consumed and CO_2 is emitted. As water is the most plentiful supply for hydrogen, it would be desirable for both the environment and the worlds energy challenge to use the suns energy, to split water in order to produce hydrogen. There are three possible ways of producing hydrogen using the sun as energy source. [5]

- Electrolysis of water, powered by a solar cell
- Reforming of biomass
- Water splitting by photoelectrochemical or photocatalysis

In the early 1970s, it was discovered that water could be split into H_2 and O_2 with UV illumination. The system was a photoelectrochemical cell consisting of TiO_2 and Pt, were they act as a cathode and anode respectively.

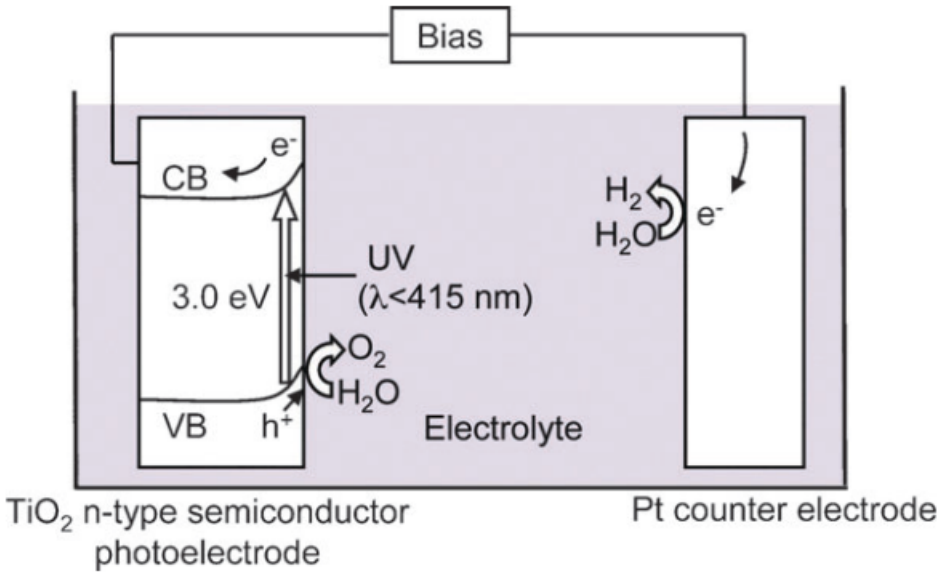

Figure 1.1: Illustrates the Honda-Fujishima effect, splitting water with a TiO_2 photoelectrode. Reproduced from [6]

This is known as the Honda-Fujishima effect, shown in figure 1.1. Some years later, the concept of this system was applied to introduce a photocatalytic process. Powdered photocatalytic systems, shown in figure 1.2, are advantageous for large-scale application of splitting water, using solar energy because of the simplicity. Photon energy conversion using powdered photocatalysts is not yet at the stage of practical use due to low energy conversion. Because photocatalytic water splitting has the potential to contribute to an ultimate sustainable solution to both energy and environmental issues, the topic needs to be investigated further. [6], [7]

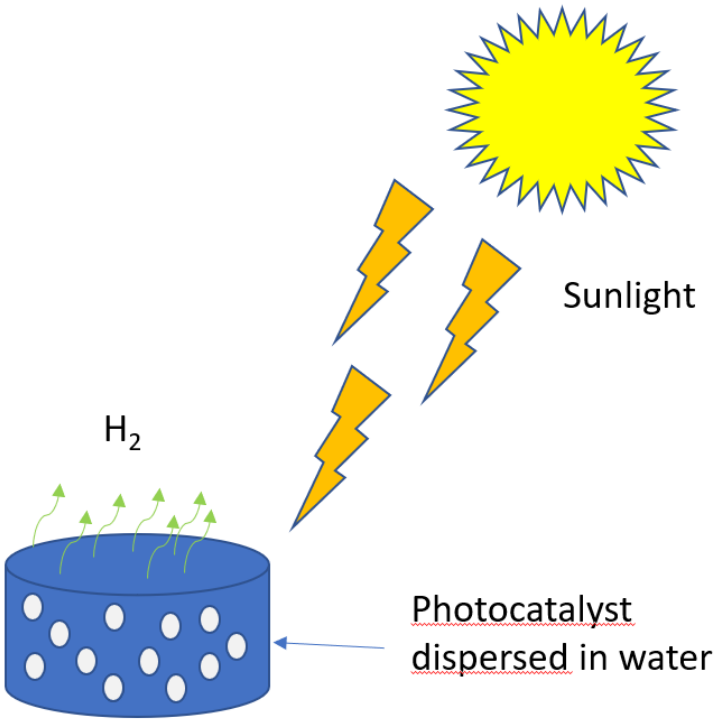

Figure 1.2: Illustrates how hydrogen can be produced from sunlight with a powdered photocatalyst. Adapted from [6]

1.1 Goal

Previous studies have shown that $SrTiO_3$ doped with Rh is active in the visible light region [6], [8]–[10]. This study will synthesize the rhodium doped $SrTiO_3$ and try to further improve the performance of the photocatalyst with carbon quantum dots. There has previously been done a study to find the optimal amount of Rh to dope $SrTiO_3$ with, for H_2 evolution from an aqueous solution of methanol under visible light irradiation. The optimal amount was then found to be 1% Rh. 0,5 wt% of Pt was used as co-catalyst. [8]

1.2 Strategy

Pure $SrTiO_3$ loaded with Pt will be tested and used as a baseline. Rh doped $SrTiO_3$ will then be tested for comparison to verify the increase in activity compared to pure $SrTiO_3$. When the activity increase has been verified, Carbon quantum dots will be loaded on to the photocatalyst, and the effects will be investigated.

1.3 Introduction to photocatalysis

1.3.1 Heterogeneous photocatalysis and conventional heterogeneous catalysis

The steps in conventional heterogeneous catalysis, shown in figure 1.3, proceeds in the following order. [11]

1. Mass transfer of the reactant from the bulk to the external surface of the catalyst
2. Mass transfer of the reactant into the pores, from the external surface.
3. Adsorption of the reactant on to the surface of the catalyst
4. Surface reaction
5. Desorption of the product from the surface
6. Mass transfer of the product to the catalysts external surface
7. Mass transfer of the product to the bulk from the external surface of the catalyst.

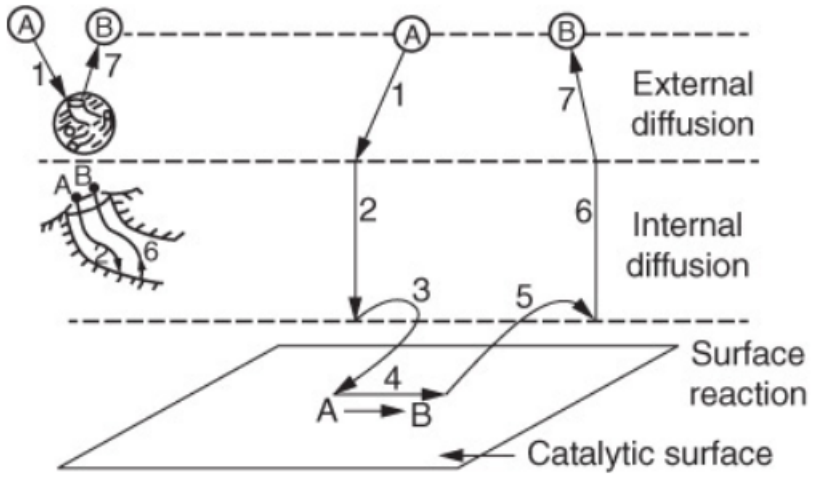

Figure 1.3: Shows the steps in conventional catalysis. The figure is reproduced from [11]

In heterogeneous photocatalysis the same steps are involved. The difference is step 4, surface reaction. Step 4 is a redox reaction, caused by electron holes in the valence band and electrons in the conduction band due to the irradiation. In heterogeneous photocatalysis the photocatalyst is often a semiconductor [6].

1.3.2 Semiconductor

Materials in solid-state can be grouped as insulators, conductors and semiconductors.

Insulators have very low conductivity, typically ranging between 10^{-18} $\frac{S}{cm}$ to 10^{-8} $\frac{S}{cm}$. Conductors have a high conductivity typically in the range of 10^{4} $\frac{S}{cm}$ to 10^{6} $\frac{S}{cm}$. Semiconductors are ranging between conductors and insulators, illustrated in figure 1.4. The semiconductors conductivity is in general sensitive to illumination, temperature, magnetic field and very small amounts of impurity atoms (typically 1 μ to 1 gram of impurity atoms per Kg of semiconductor). [12]

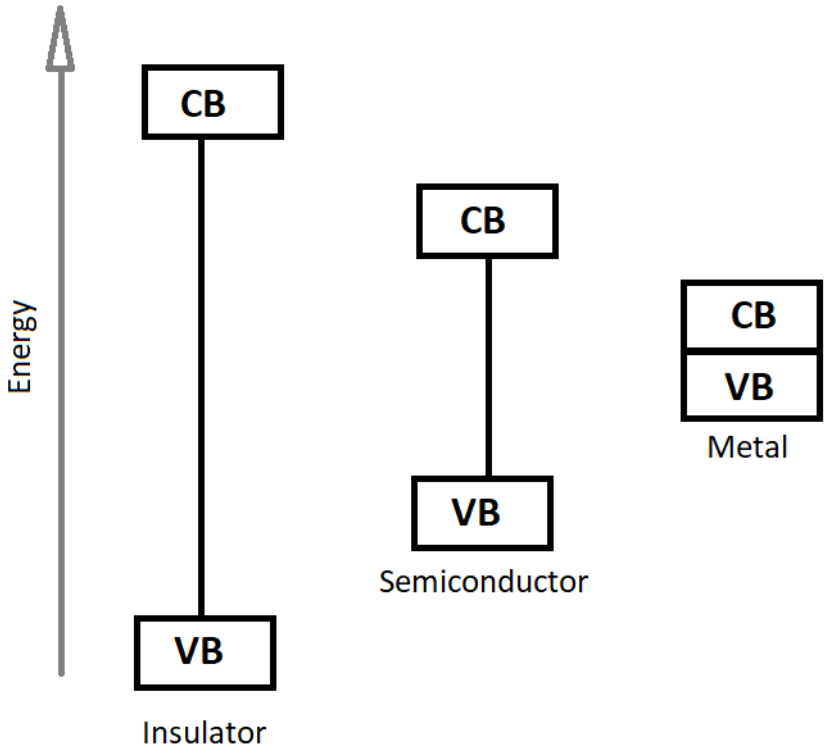

Figure 1.4: Illustrates the band gap of the different materials. adapted from [13]

The way the electrons energy levels is arranged in a semiconductor gives the semiconductor properties between insulators and metals. When an atom is isolated, electrons are found in definite states were each state is separated by discrete quanta of energy [14]. In a solid, Broad energy bands is formed by interaction between the molecular orbitals. The semiconductors electronic structure is characterized by a Valence band (VB) and a Conduction band (CB), and between these bands, there are no energy levels. The VB is filled with electrons, and the CB has no electrons. Between the highest energy level in the VB and the lowest energy level in the CB, the energy difference is known as the band gap energy (Eg). When the semiconductor absorbs a photon with energy equal to or exceeding the band gap, an electron is excited from the VB up to the CB. The VB now has an electron vacancy known as an electron hole (h^+). [15]

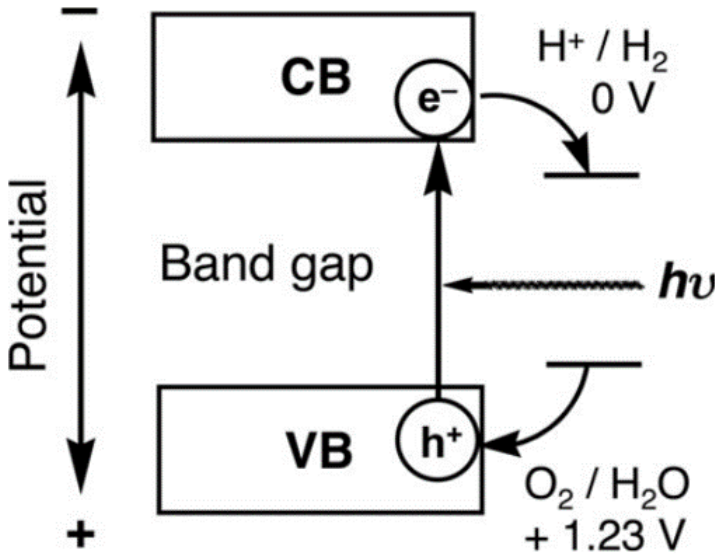

Figure 1.5: Shows the principle of band gap and reduction/oxidizing potential. The figure is reproduced from [6]

A semiconductor can be used as a photocatalyst because, when it absorbs a photon with high enough energy, simultaneous reduction and oxidizing reactions can occur on the semiconducters surface, illustrated in figure 1.5 [16]

1.3.3 Quantum Yield

Quantum Yield is equal to the ratio of the reaction rate with the unit, molecules converted per second, divided by the incident photonic flux, with the units photons per second, shown in equation 1.1. This kinetic definition is directly related to the efficiency of a photocatalytic system. One Einstein is equal to one mole of photon, hence the unit of Quantum Yield can also be written as moles per second divided by Einstein per second, as is also shown in equation 1.1. The maximum value of Quantum Yield is equal to 1. The Quantum Yield is affected by the following factors: [15], [17]

- The nature of the photocatalyst
- Experimental conditions

- The nature of the reaction that is being studied

These paramaters is fundamental to have knowledge of as they enable:

- comparison of catalytic activity of different photocatalysts for the same reaction
- Estimate the feasibility of different reactions
- calculate the energetic yield of the process

$$\text{Quantum Yield} = \frac{\text{Reaction rate}}{\text{Effecient photonic flux}} \left[\frac{\text{molecules/s}}{\text{photon/s}}\right] or \left[\frac{\text{moles/s}}{\text{Einstein/s}}\right] \tag{1.1}$$

1.3.4 Photocatalytic reaction process

As mentioned earlier the mass transfer for photocatalysis is similar to conventional catalysis but, step 4 is different. Many photocatalysts have semiconductor properties and the photocatalytic reaction, for water splitting, proceeds on semiconductor materials as depicted in figure 1.6. [6]

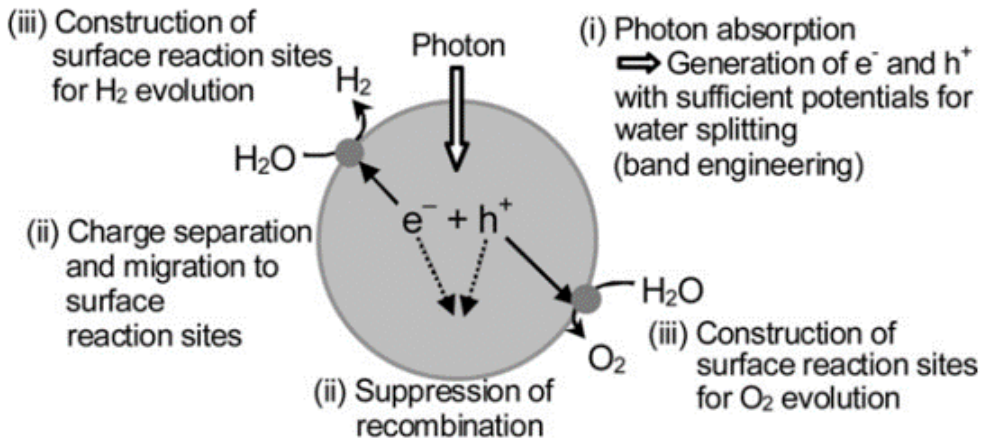

Figure 1.6: Shows an overview of the process in photocatalytic water splitting. Reproduced from [6]

Electrons are generated in the CB and holes are generated in the valence band when the incident light has larger energy than that of the band gap. Redox reactions are caused

by the photogenerated holes and electrons similarly to electrolysis. H_2O molecules are reduced and oxidized to form H_2 and O_2, respectively, for overall water splitting. The width of the band gap and the level of the valence bands and conduction bands are important points for photocatalytic materials with semiconductor properties. In the CB the lowest level has to be more negative than the redox potential of H^+ / H_2O and the highest level in the VB need to be more positive than the redox potential of O_2 / H_2O. The theoretical minimum band gap for a photocatalyst, able to split water, is therefore 1,23 eV which corresponds to light of approximately 1000 nm. [6]

In figure 1.6, the second step consists of charge separation and migration of photogenerated carriers. Crystallinity, crystal structure and the size of the particles are strongly affecting the step. With an increase in the crystalline quality, there is a decrease in the amounts of defects. The defects are decreasing the photocatalytic activity because they operate as trapping and recombination centers between the photogenerated electrons and holes. By a decrease in the particle size, the migration distance for photogenerated electrons and holes becomes smaller which in terms results in a decrease in the probability of recombination. [6]

The important point in the third step, in figure 1.6, is the active sites and surface area. The photogenerated electrons and holes will recombine if the active sites for redox reactions don't exist on the surface. Co-catalysts can be loaded on to the surface of the photocatalyst to introduce active sites. Typical co-catalysts can be Pt, NiO and RuO_2 [6]

Chapter 2

Theory

To implement photocatalysis successfully requires a reactor, illumination sources and the photocatalysts to be efficient. It is also important to assess the photocatalytic reactor's effectiveness and the kinetic reactor modeling. If it is an artificially powered photoreactor, the photons absorbed in the photoreactor and the near-UV lamps need to be appropriately characterized.
The definition of a photocatalyst is, a substance activated by the absorption of a photon and accelerates a reaction, without being consumed itself. The activity of a photocatalyst is influenced by the structure of the catalyst, spectral activation, particle size, surface properties and mechanical stresses. There is of course, also the factor of the preparation itself. [18], [19]

2.1 Materials

Figure 2.1 shows band levels in different semiconductors and the related redox potential for water splitting. $KTaO_3$, ZrO_2, TiO_2 and $SrTiO_3$ has a band gap that is suitable for water splitting. These materials are, according to literature, active for water splitting when modified with a co-catalyst. CdS also seem to have a suitable band structure for water splitting, but instead of H_2O getting oxidized, the S^{2-} is

getting oxidized by the photogenerated holes. This also leads to the elution of $Cd2+$ shown in equation 2.1. This can also happen to ZnO under bandgap excitation, shown in equation 2.2, and the reaction is called photocorrosion. As shown with ZnO, photocorrosion can happen even if the photocatalyst is an oxide. Photocorrosion can be avoided if a $holescavanger$ exist. [6]

$$CdS + 2h^+ \rightarrow Cd^{2+} + S \tag{2.1}$$

$$ZnO + 2h^+ \rightarrow Zn^{2+} + \frac{1}{2}O_2 \tag{2.2}$$

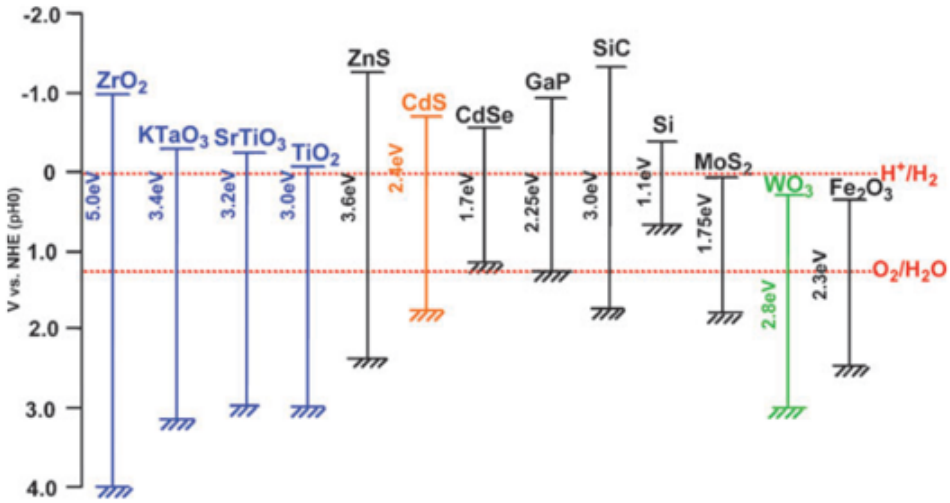

Figure 2.1: Shows the potential for different semiconductors in regards to water splitting

2.1.1 Elements for constructing a photocatalyst

Elements for constructing a heterogeneous photocatalyst are divided into four groups. (I) Is for constructing a crystal and energy structure. (II) is only for constructing crystal structure. (III) can be used to form impurity levels as dopants. (IV) Co-catalytic

elements. An overview is presented in figure 2.2. [6]

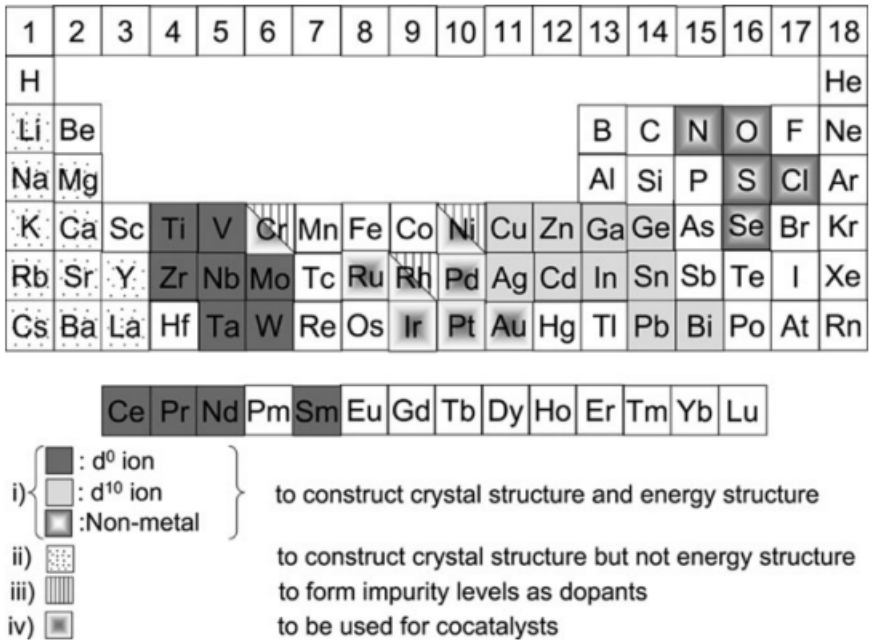

Figure 2.2: Elements for constructing a heterogeneous photocatalyst. Reproduced from [6]

2.1.2 Strontium titanate

As mentioned above, Strontium titanate possess a suitable band gap and is active for water splitting. Though the strontium titanate is photocatalytically active, it has a large band gap and is therefore only active in the UV region. As the suns radiation specter reaching earth's ground is only 4-5 % UV [20] and the visible region is approximately 43 %, shown in figure 2.3, it is desirable that the photocatalyst is active in the visible light area [21].

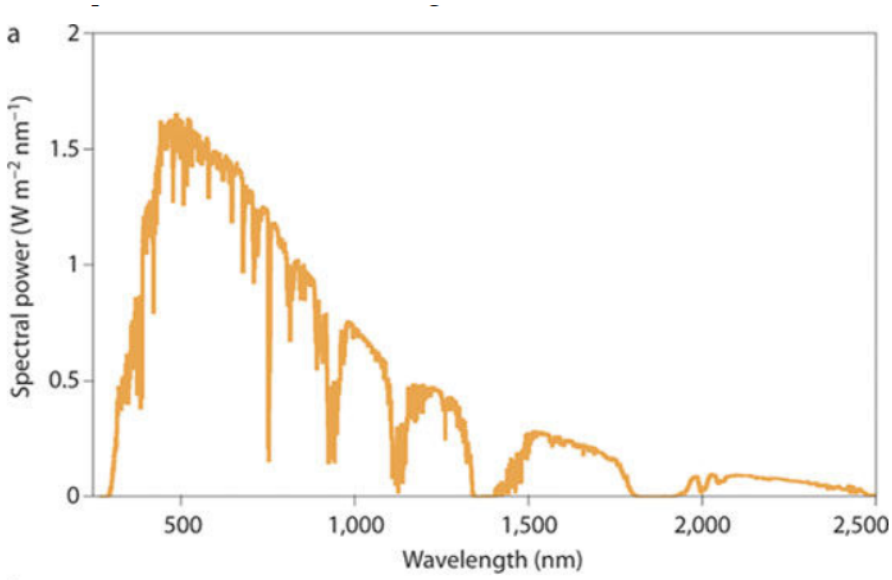

Figure 2.3: The Sun's power spectrum reaching the Earth. Reproduced from [22]

Previous studies have shown that $SrTiO_3$ is active in the visible light area when doped with Rh [6], [8], [23], [24]. The optimal amount of Rh to dope the $SrTiO_3$ with has previously been found to be 1% with the stoichiometric balance shown in equation 2.3. This experiment was performed with methanol as the sacrificial reagent. [8]

$$Sr : Ti : Rh \rightarrow 1 : (1-x) : x \tag{2.3}$$

In addition, to contribute to visible light absorption, the Rh dopant also acts as a recombination center for the photogenerated holes and electrons. Hence the photocatalytic efficiency is determined by the balance of these factors. [24]

2.2 Synthesis

2.2.1 Solid state reaction

In addition to hydrothermal synthesis and the sol-gel method, the conventional solid state reaction is among the most common methods to synthesize solid oxide

photocatalysts [25], [26]. For preparing polycrystalline solids, the solid state reaction is the most widely used method. The procedure is fairly simple as it involves mixing the precursor followed by grinding and calcination in repeated cycles. The disadvantage with solid state method is that it results in poor uniformity and large particle size due to the high-temperature treatment. This reduces the particle surface area, and hence the photocatalytic activity is decreased. [27]

2.2.2 Other common preparation methods for photocatalysts

Hydrothermal method

The nanoparticles produced by the hydrothermal method, have a significant degree of crystallinity. This is very beneficial for thermal stability of synthesized materials. However, achieving precise control over all the reaction parameters is a challenge. [27]

Sol-gel method

Preparation by the sol–gel method is involving, hydrolysis-condensation of metal-alkoxides, concentration of aqueous solutions containing metal-chelates and organic polymeric gel routes. In sol-gel method, controlling the homogeneity of different components during the process is difficult due to the hydrolysis rate of the metal alkoxides being fast. [27]

2.2.3 Incipient wetness impregnation

Incipient wetness impregnation is a method for depositing an active component, such as Pt, on to the surface of another component. Impregnation, drying, and calcination is the three steps in this process that governs the obtained load and distribution of the active component. [19]

In the impregnation step, the precursor is mixed with a solution so that the volume of the solution is equal to the pore volume of the support. The solution, containing the precursor with the desired amount of the active component, is then pulled into

the pores of the support material by capillary forces. If the impregnation is executed correctly, there should be no excess liquid [28]. The volume of the solution can be calculated from N_2 physisorption, but this technique may be uncertain. A more reliable method would be to drip deionized water on the support until it reaches saturation, to find the volume of the solution empirically [29].

If the volume of the solution exceeds the pore volume of the support material, the deposition process is called "wet impregnation".[30], [31]

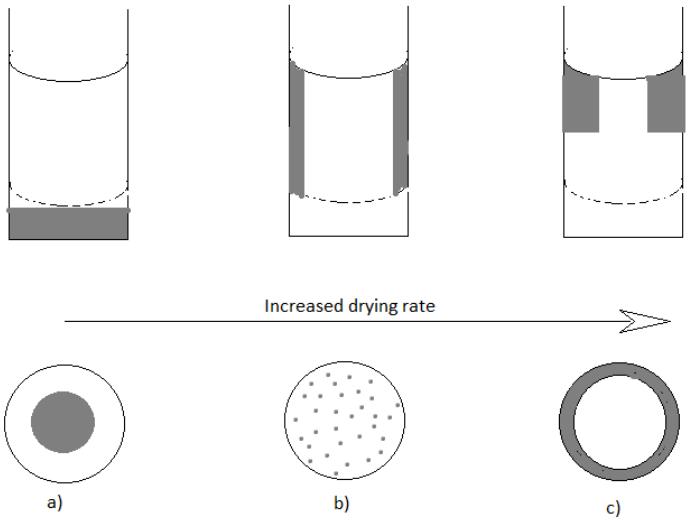

Figure 2.4: Illustration of how the drying rate affects the distribution of the active component. In a) the drying rate is to slow. b) represents an ideal drying rate and in c), the drying rate is to fast. The figure is adapted from [29]

The drying step crystallizes the metal salt onto the pore surface. During the drying process, the saturation of the precursor compound in the liquid solution is increased to the point of crystallization [28]. The drying rate affects the distribution of the active component, within the pore. The ideal drying rate is identified when the active component is dispersed evenly on the support, as shown in figure 2.4 b). If the drying rate is too fast, the active component is crystallized at the pore opening because the evaporation is driven from inside the pores. The result is illustrated in figure 2.4 c).

A drying rate which is to slow results in most of the salt crystallizing at the bottom of the pores, illustrated in figure 2.4 a). This is due to the evaporation occurring at the meniscus of the solvent causing it to migrate to deeper into the pore. The third and last step is calcinating the sample, to convert the crystallized precursor salt into a metal or a metal oxide and prevent it from redissolving if the sample is exposed to humid environment.

2.2.4 Photodeposition

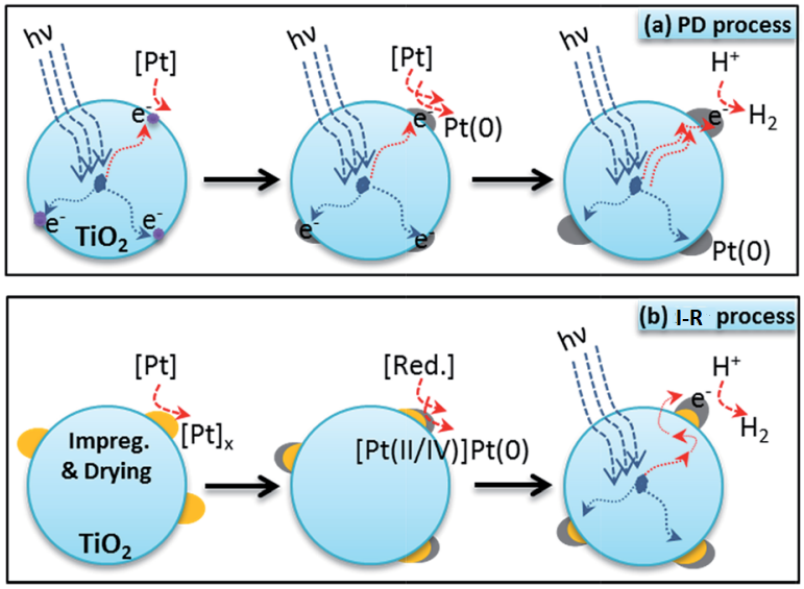

Figure 2.5: Illustrates the photodepostion vs I-R of Pt. Reproduced from [32]

Another method, in addition to impregnation, for loading metal on to a photocatalyst is by photodeposition. The method is more convenient than impregnation and yields a well dispersion of the metal, only in the elemental state, and subsequently the rate of H_2 evolution is higher than samples prepared by impregnation [32] [33]. 2.5b) illustrates the process of depositing Pt on to a photocatalyst by impregnation.

In photodeposition, the Pt is selectively deposited on the e^- trapping sites through an internal-to-external reduction process. The process for Pt photodeposition is

illustrated in 2.5a) and can be described as follows. 1) after being activated by a photon, with high enough energy, the photo-induced e^- will migrate from the bulk to the surface and then be trapped by surface trapping sites. 2) The Pt precursor near the e^- sites is then reduced to Pt(0) and deposited exactly on the sites. 3) The Pt cluster then serves as new e^- sinks and loading sites to carry on the deposition. [32]

For 2.5b) the precursor, for the Pt, is loaded on to the photocatalyst by impregnation and drying process. Upon the evaporation of water, the precursor is loaded randomly on the photocatalyst and aggregates in the late stage due to the concentration of the impregnation solution. The precursor is then reduced to metallic Pt by an external reductant, e.g., H_2. The reduction occurs from external to internal sites, in contrast to the photodeposition. Once the outer layer is reduced to Pt(0), it will hamper the reduction of the interior. [32]

2.3 Gas chromatography, (GC)

The principles of gas chromatography; an inert carrier gas flows through the injection port, column, and detector. The carrier gas has a carefully controlled flow rate to ensure reproducible retention times and to minimize detector drift and noise. The sample is injected into a heated injection port and carried into the column. The sample is separated into individual components based on relative solubility in the liquid phase and relative vapor due to partitions between the mobile and stationary phases in the column. The carrier gas, with the separated sample, then flows through a detector. The detector then measures the quantity of the sample and generates a signal. This signal goes to a data system that generates a chromatogram. [34] [35]

Mobile and stationary phase

The carrier gas is the mobile phase in the GC. The carrier gas is chemically inert and flows, continuously, through the injection port, column, and detector. The purpose of the carrier gas is to carry the sample through the system without chemically interacting

with it. The mobile phase is required to be of high purity. The choice of carrier gas is dependent on the detector.

Stationary phase

In gas-liquid partition chromatography, the stationary phase is a nonvolatile liquid bonded to the inside of the column or a fine solid support [35]. In gas-solid adsorption, the analyte is adsorbed directly on to solid particles of the stationary phase [35]. The stationary phase is dependent on the type of column utilized. Open tubular columns compared to packed columns, offer higher resolution, shorter analysis time, greater sensitivity and lower sample capacity. Depending on the compounds relative adsorption on the stationary phase and the respective vapor pressures, the sample gas is separated into its individual components. The components then exit the column at different time points. The components then enter the detector that quantifies the respective compounds and generates an electrical signal that is sent to a computer system. [35] [34]

Detector

Thermal conductivity detector is one of the most common detectors. Other common detectors are flame ionization detector and electron capture detector. The thermal conductivity detector measures the thermal conductivity of the solute compound in the carrier gas and compares it to the thermal conductivity in the carrier pure gas. Thus it is beneficial to use a carrier gas that possesses different thermal conductivity properties than the sample. [34]

2.4 Mechanisms

2.4.1 Proposed mechanism

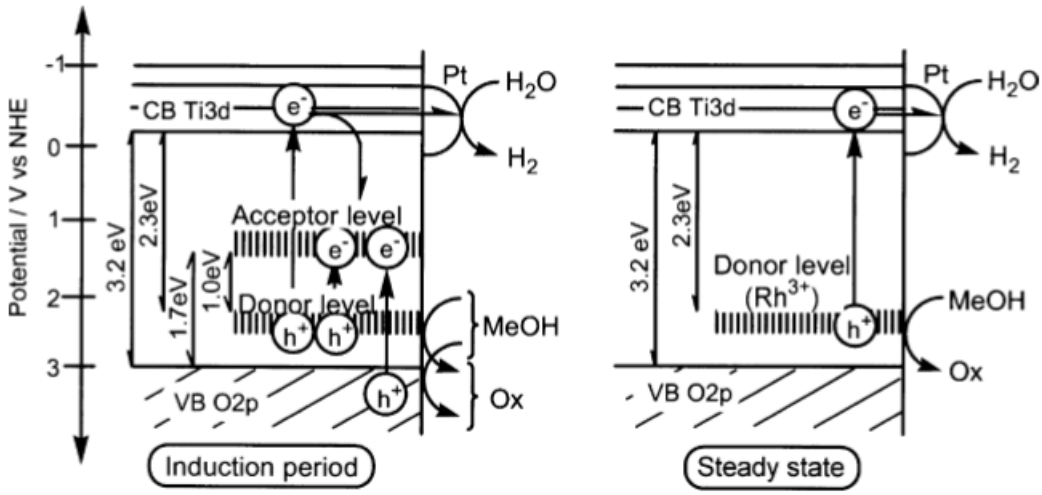

Figure 2.6: Shows the proposed band structure for $SrTiO_3 : Rh$ reproduced from [8]

Figure 2.6 illustrates how the photocatalytic evolution of H_2 proceeds on Pt loaded, Rh doped $SrTiO_3$ ($Pt/SrTiO_3 : Rh$). The doped Rh is assumed to exist in at least 2 species, Rh^{3+} and a Rh species with a higher oxidation number, e.g., Rh^{5+}. Because of the charge and distortion compensation by their cations, the Rh ions are assumed to be neighbors. Photogenerated electrons, at an early stage, can easily reduce the Rh with the higher oxidation number to Rh^{3+} indicating that it works as an electron acceptor. The $Pt/SrTiO_3 : Rh$ is highly efficient for H_2 evolution under visible light, indicating that the Rh^{3+} works as an electron donor. UV-visual absorption specter from [8] showed absorption bands around 580 nm (1.7 eV) and 1000 nm (1.0 eV) are assigned to the transition from the VB and the donor level to the acceptor level, respectively. After the reduction from the photogenerated electrons (induction period) the absorption band remaining is the transition from the donor level to the CB. [8]

2.4.2 Sacrificial reagents

In photocatalytic water splitting sacrificial reagents can be deployed to evaluate if the photocatalyst, being studied, satisfies the kinetic and thermodynamic potential for H_2 and O_2 evolution. [6]

When a reducing agent is added to the aqueous solution, it enhances the evolution of H_2 in water. The enhanced evolution of H_2 is due to the reducing agent being oxidized by the photogenerated holes instead of water. The reducing agent can also be referred to as a *hole scavenger* or an *electron donor*. Figure 2.7 (A) shows an example of the evolution of H_2 with alcohol as a sacrificial reagent. [6]

An oxidizing reagent, figure 2.7 (B), can be added to the solution to evaluate the photocatalysts thermodynamic and kinetic potential for oxygen evolution. [6]

When a sacrificial reagent is added, the reaction is regarded as a half-reaction of water splitting. It is not guaranteed that a photocatalyst that is active for these half-reactions will, in the absence of sacrificial reagents, be able to split water into H_2 and O_2. It follows that the term "water splitting" must be distinguished from H_2 and O_2 evolution from aqueous solutions where a sacrificial reagent is present. Water splitting means to split water into stoichiometric amounts of O_2 and H_2, without a sacrificial reagent.[6]

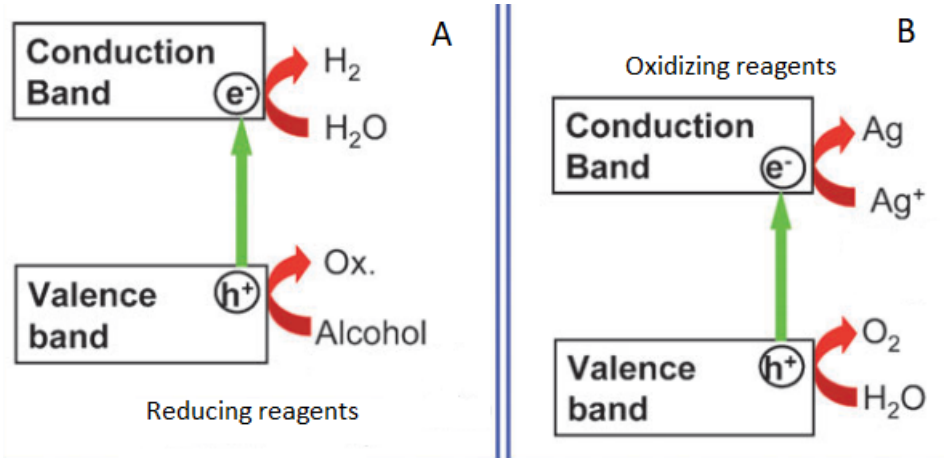

Figure 2.7: Illustrates how reducing (A) and oxidizing (B) agents help promote H_2 and O_2 evolution respectively, in water solutions. Reproduced from [6]

2.4.3 Carbon quantum dots (CQDs)

CQDs was first discovered in 2004 in a report on components of fluorescent nanoparticles derived from singlewall carbon nanotubes. [21], [36]

Carbon quantum dots is a novel class of carbon nanomaterials with fluorescence which is prominent. The material is composed of discrete quasi-spherical carbon nanoparticles, and the sizes are below 10 nm. The CQDs is distinguished from other traditional semiconductor quantum dots because the CQDs can integrate optical properties with electronic properties of carbon materials. [21]

CQDs posses a potential in photocatalysis due to being superior in water solubility, chemical stability and it is showing low toxicity towards other common photocatalysts, e.g., TiO_2, ZnO and CdS. After specific surface modification, CQDs has an excellent and tunable property of absorbance and photoluminescence. The upconverted photoluminescence of CQDs is an optical phenomenon, where materials emit light with smaller wavelength than the excitation source. This phenomenon can extend the sunlight absorption of semiconductors with wide band gaps into the visible light region. An illustration of how the CQD's upconversion can improve the photocatalytic activity of a photocatalyst is shown in figure 2.8, reproduced from [37] CQDs, are also excellent electron acceptors and electron donors, when photoinduced. This results in efficient separation of holes and electrons. [21], [38], [39]

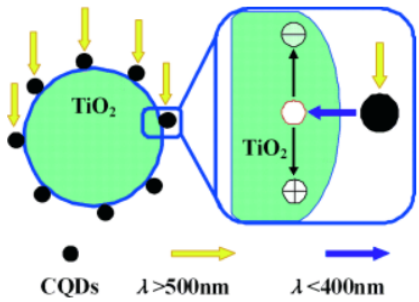

Figure 2.8: Illustrates how the CQD's can improve the photocatalytic activity of TiO_2 by upconverting the light. Reproduced from [37]

2.4.4 Upconversion

Photon absorption

The author has not been able to obtain a mechanism for the upconversion for CQD's. Instead, an example of upconversion reproduced from [35] is presented.

Fluorscence; Photon emission from a transition between states with the same quantum numbers. **Phosphoricescence**; Photon emission from a transition between states with different quantum. **Intersystem croossing**; a transition between two different spin quantum numbers without radiation. **Internal conversion**; Is a transition between states with the same quantum spin number without radiation.

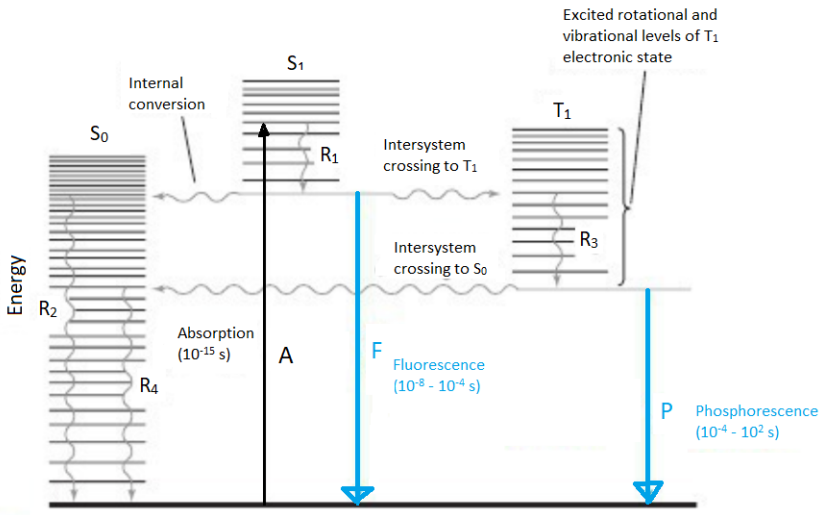

Figure 2.9: Illustrates physical processes that can occur when a molecule absorbs a photon. Processes involving photons are represented by straight arrows and transitions without radiation are represented with wavy arrows. S_0 is the ground electronic state. S_1 and T_1 is the lowest excited singlet and triplet electronic state. Figure is reproduced from [35]

The process labeled R_1 in 2.9, illustrates vibrational relaxation which is a radiationless transition where energy is transferred to other molecules through collisions. The net

effect is, part of the energy absorbed from the photon is converted to heat. In this process, the photon promotes a molecule from ground electronic state, S_0 to a level which is excited vibrationally and rotationally of the excited electronic state S_1. The molecule could also emit a photon after the vibrational relaxation. The photon that is emitted from the radiational transition, S_1 to S_0 is fluorescence. [15], [35]

If the molecule follows the path from A to R_1 then follows up with an internal conversion to R_2, in figure 2.9, all of the energy absorbed from the photon will have been converted to heat. If the molecule crosses from S_1 into an excited vibrational level of T_1 (Intersystem crossing), some of the energy will be converted heat, R_3. From R_3 a radiationless path can occur through a second intersystem crossing to S_0 followed by R_4 in 2.9 where, again, all the energy is converted to heat. Another path that can occur is that the energy, after R_3 is emitted as a photon. The radiational transition from T_1 to S_0 is called phosphorescence.[15], [35]

Upconversion mechanism

Figure 2.10: Shows a green laser shining on a solution, containing ruthenium(II) complex and a 9,10-dphenylantharacene, that is upconverting green photons to blue photons. Reproduced from [40]

Because part of the excitation energy is converted to heat, as shown in 2.9 R_1 and R_3, due to vibrational relaxation, the fluorescence and phosphoric escence usually come at a lower energy than the excitation energy. In figure 2.10 a green laser is shined upon a solution containing ruthenium(II) complex and a 9,10-dphenylantharacen, shown in figure 2.11, and green photons are upconverted to blue photons. The energy balance is preserved because the reactions require two green photons per blue photon. [35]

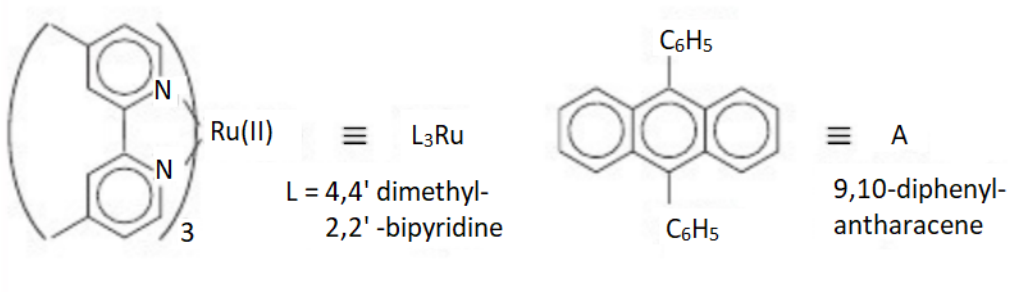

Figure 2.11: Shows the ruthenium(II) complex and a 9,10-dphenylantharacen. Reproduced from [35]

When a green photon is absorbed, the L_3Ru is promoted from the ground state, S_0, to its excited state, S_1. The excited singlet state then decays to the triplet state T_1. Equation 2.4. The excited state is denoted with an asterisk (*) in equation 2.4, 2.5, 2.6 and 2.7. [35]

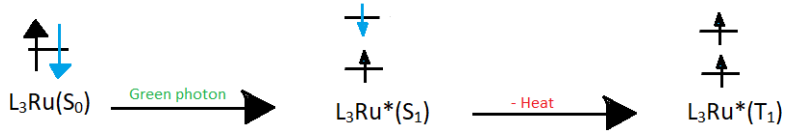

(2.4)

In the absence of O_2, the excited triplet $L_3\text{Ru}^*(T_1)$ is relatively long-lived. The excitation energy can be transferred to ground state anthracene and excite it to a triplet state. Equation 2.5. [35]

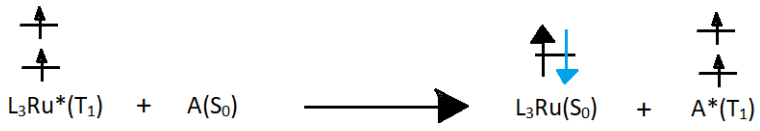

(2.5)

In equation 2.6, two excited triplet anthracene collides where one is promoted to the

excited singlet state S_1, and the other is demoted to ground state. [35]

The reaction between $L_3Ru(T_1)$ and $A(S_0)$ preserves the electron spin angular momentum, with two spins up and two spins down in reactants and products. The reactions that conserve the spin angular momentum are, in general, faster than reactions where the spin is changed. The spin angular momentum is also conserved in the reactions shown in equations 2.6 and 2.7. [35]

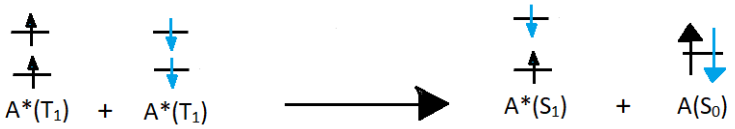

(2.6)

To return to the ground state the excited singlet anthracene can emit a blue photon. Equation 2.7. [35]

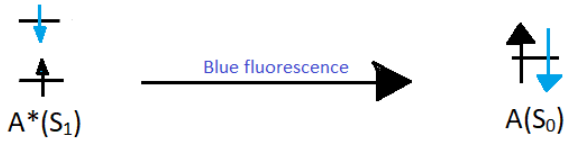

(2.7)

The result of these reactions are two green photons, absorbed by $L_3Ru(II)$, being converted to one blue photon emitted by anthracene. The measured quantum yield is 3,3 % for this process. [35]

2.5 Characterization

2.5.1 Physisorption

The principle for measuring the surface area is to physisorb an inert gas, e.g., nitrogen or argon. The surface area is then found by determining the number of molecules

needed to cover the entire surface with a monolayer. Though the principle is easy, there are a few complications connected to this method such as multilayer adsorption and the inert gas condensing into smaller pores. The B.E.T equation is shown in equation 2.8. It is derived from several assumptions and describes the relationship of the volumes between the adsorbed gas, at a given partial pressure and the monolayer coverages volume. [19]

$$\frac{P}{V_a \cdot (P_0 - P)} = \frac{1}{XV_0} + \frac{X-1}{XV_0} \cdot \frac{P}{P_0} = \eta_p + a\frac{P}{P_0} \tag{2.8}$$

The $\frac{P}{V_a \cdot (P_0 - P)}$ can be plotted against $\frac{P}{P_0}$ to get a straight line, the slope is then, a= $\frac{X-1}{XV_0}$ and the η_p = $\frac{1}{XV_0}$ will be the crossing of the y-axis. V_0 = $\frac{1}{a+\eta}$ is the volume of the first monolayer adsorbed to the catalysts surface and it is possible to calculate the number of molecules adsorbed from this volume by N_0 = $\frac{PV_0}{k_b T}$. The total area can be found, if the size of the area one molecule fills, is known, by A_p= N_0 A_0 [19]

According to [19], the BET method has limitations, and there are improvements that exist, but states that the BET isotherm under the following assumptions, is valid [19]

- The adsorption and the desorption rate are equal.
- The adsorption sites are equivalent for the molecules adsorbed in the first layer.
- The first layer of molecules constitutes the adsorption sites for the molecules adsorbed in the second layer. The second layer of molecules then does the same for the molecules in the third layer and so on.
- Interactions between adsorbate-adsorbate is ignored
- All the adsorbed layers, except the first, have the same adsorbed-desorbed conditions.
- The condensation energy is equal to the adsorption energy from the second layer and higher of adsorbed molecules.
- At saturation pressure, the multilayer will grow towards infinite thickness.

2.5.2 X-ray fluorescence

The process in X-ray fluorescence analysis can, simplified, be considered in three steps occurring at atomic level. An electron is knocked out from one of the nucleuses surrounding orbitals, within the atom of the material, by an incoming X-ray. This produces a hole in the orbital which results in high energy and an unstable configuration for the atom. An electron from an outer orbital, with higher energy, falls into the hole to restore the equilibrium. Because the electron falls into a position of lower energy, fluorescent X-ray is emitted to discard the excess of energy. The difference in energy from the orbital where the hole was created and the orbital from where the electron came to fill the hole, is characteristic for each element atom. Therefore the emitted fluorescent X-ray is directly linked to the element being analyzed. For a particular element, the energy in the X-ray emitted is independent of the materials chemistry. [41], [42]

2.5.3 Ultraviolet and visible light spectroscopy

The definition of a photocatalyst states that a photocatalyst is activated upon the absorption of a photon; thus it is important to be able to estimate the number of photons absorbed by the photocatalyst [18]. UV-visible spectroscopy is a well established characterization method within catalysis [19]. The technique can reveal information about molecular species, particles, and extended structures from examining the electronic transitions. From exciting photons, information about the chemical bonds, coordination and oxidation degree can be obtained. The technique is performed under gaseous atmosphere, and a quantitative analysis is possible. It is also applicable to solids containing transition metals. [43]

Because the electrons in the outer shells are driven to the excited energy levels by electromagnetic radiation in the spectral region, this type of spectroscopy is often called electronic spectroscopy. For liquid and gas phases, the optical spectroscopic measurements are conducted in transmission mode, while a technique called diffuse reflectance spectroscopy is used for investigating solids and powders. DRS is a

technique for measuring the reflectance spectra at different wavelengths instead of the photoabsorption [44], [45]. [46]

The reflectance spectra can be transferred to the equivalent absorption spectra with Kublka-Munk function, shown in equation 2.10. R_∞ is constant and represents the limit of reflection factor when the thickness of the solid reaches infinite [45]. R_∞ can be found from equation 2.9, where R_{sample} is the reflectance value of the sample and $R_{reference}$ is the reflectance value of the of the reference material. A is the absorption coefficient, S represents the scattering coefficient and is assumed to be constant. [45], [47]

$$R_\infty = \frac{R_{sample}}{R_{reference}} \tag{2.9}$$

$$F(R_\infty = \frac{1-R_\infty)^2}{2R_\infty} = \frac{A}{S} \tag{2.10}$$

$$A \propto \frac{(h\upsilon - E_0)^\eta}{h\upsilon} \tag{2.11}$$

Equation 2.11 shows the energy dependence of the absorption factor near the absorption edge. E_0 is the optical absorption edge energy, $h\upsilon$ is the photon energy, η is a factor dependent on the optical transition caused by the photon absorption. To find the band gap energy or optical absorption energy of the sample, $(A \times h\upsilon)^{1/\eta}$ can be plotted against $h\upsilon$. The result will be linear near the edge energy. The linear part can then be extrapolated to $(A \times h\upsilon)^{1/\eta} = 0$; the corresponding value is the band gap energy. [45], [47]

2.5.4 X-ray diffraction

X-ray diffraction is a technique which is frequently being used in catalyst characterization. XRD is performed by illuminating the sample with monochromatic X-ray beams to form structural interference. This technique can give information

about the particle size and find crystalline phases in the catalyst. Using Bragg's law, the lattice spacings can be derived. [8, 9] An illustration is shown in figure 2.12, reproduced from [19]

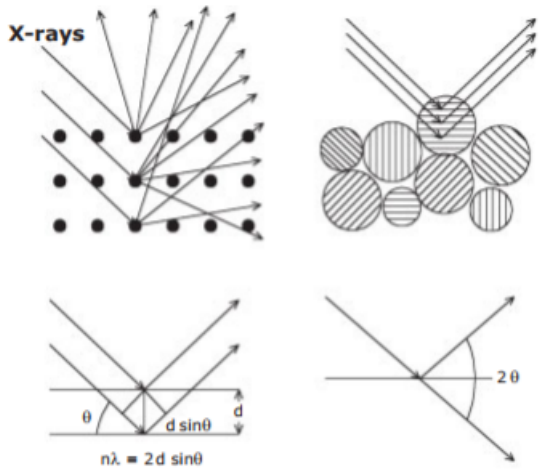

Figure 2.12: 1 Illustrates the X-ray's hitting and being reflected, forming structural interference. Reproduced from [19]

$$n\lambda = 2dsin(\theta) \tag{2.12}$$

n is an integer which represents the order of reflection

λ is the X-rays wavelength

d is the the length between two lattice planes

θ is the angle the X-ray beam hits the reflecting lattice plane

If the general case of hkl planes is considered, equation 2.12 can be rewritten as[19], [23], [48]

$$\lambda = 2d_{hkl}sin(\theta_{hkl}) \tag{2.13}$$

The clear diffraction peaks can be observed, only if the sample possess sufficient

long-range order, which is an important limitation to XRD. This limitation offers an advantage, which is that the width of the diffraction peak is carrying information about the reflecting plane's dimensions. Incomplete destructive interference causes line-broadening If the crystallite size is below 100 nm [23], [48]

From the diffractograms it is possible to find the particle size by using the Scherrer equation, equation 2.14

$$< L >= \frac{K\lambda}{\beta cos(\theta)} \tag{2.14}$$

$< L >$ is the particles measured dimension in the perpendicular direction of the reflecting plane

K is constant

β is the width of the peak

2.5.5 ICP-MS

Inductively
Coupled Plasma Mass Spectrometer (ICP-MS) was commercially introduced in 1983 and is an analytic technique, used for determining elements. ICP-MS is a combination of a high-temperature source (ICP) and a mass spectrometer (MS). The atoms in the elements are converted to ions in the ICP. The ions are then separated and detected by the mass spectrometer. [49]

Inductively coupled plasma

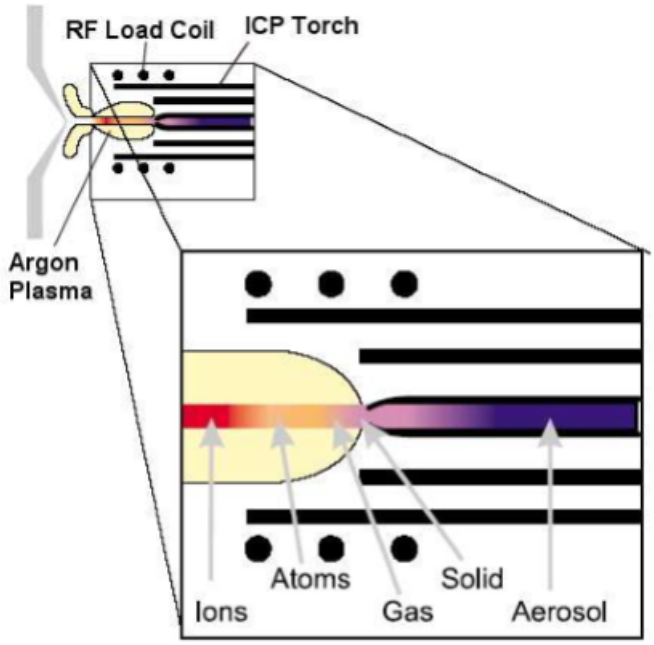

Figure 2.13: Shows the ICP torch. Figure is reproduced from [49]

In figure 2.13 a schematic of an ICP source for an ICP-MS is represented. In the ICP torch's concentric channels, argon gas is flown. A radio frequency generator is connected to the RF load coil. As the generator supplies the load coil with power, oscillating magnetic and electric fields are established at the end of the torch. When the argon flowing through the torch is exposed to a spark, argon ions are formed because the electrons are stripped off the argon atoms. The ions are the caught in the oscillating field where they collide with other argon atoms and form an argon plasma, maintaining a temperature of 6000 to 10 000 [K]. The quartz torch is protected from overheating by argon coolant gas. The ICP discharge typically forms positive ions making elements that prefer to form negative ions hard to detect. [49]

Mass spectrometer

The plasma ionizes the atoms, which is further passed into a mass spectrometer where the ions are separated by their mass-to-charge ratio, and then the quantity is measured. [35] [49]

The fundamental purpose of the detector is to translate the number of ions striking the detector into an electrical signal that can be measured and related to the number of atoms in the sample. [49]

The type of mass spectrometer which is most common is the quadrupole mass filter. The quadrupole mass filter can separate up to 2400 AMU (atomic mass units) per second. [49]

Chapter 3

Experimental

3.1 Catalyst preparation

Materials purchased for this project was

- $SrCO_3$, (≥ 99.9 %)
- TiO_2-P25 (≥ 99.5 %)
- Rh_2O_3 (99.8 %)

The materials was purchased from Sigma Aldrich and used as received. In addition there was used a solution of carbon quantum dots prepared externally from this project. There was also a solution of Pt nitrate which was diluted to a concentration of 0,002 $\frac{gramPt}{ml}$ before usage.

3.2 Preparation strontium titanate

The preparation method that was used was the solid state reaction method, the procedure is depicted in figure 3.1. Amounts of $SrCO_3$, TiO_2 and Rh_2O_3 necessary to achieve the desired amount of photocatalyst were mixed and then crushed with a

mortar and pestle. The sample was then submitted for 2 hours calcination in static air, using a high temperature furnace. The sample was then crushed again and submitted for 10 hours calcination in static air.

Table 3.1: Overview of the grinding (Time) and calcination temperature. The pre calcination was 2 hours for all samples and the final calcination was 10 hours for all samples

Batch	**Grinding [min]**	Pre calcination [°C]	**Grinding [min]**	**Final calcination** °C
Batch 1	30	600	30	1000
Batch 2	30	600	30	1000
Batch 3	50	600	50	1000
Batch 4	40	600	40	1000
Batch 5	40	600	40	1000
Batch 6	-	-	30	1000
Batch 7	-	-	50	1000
Batch 8	40	600	40	1100

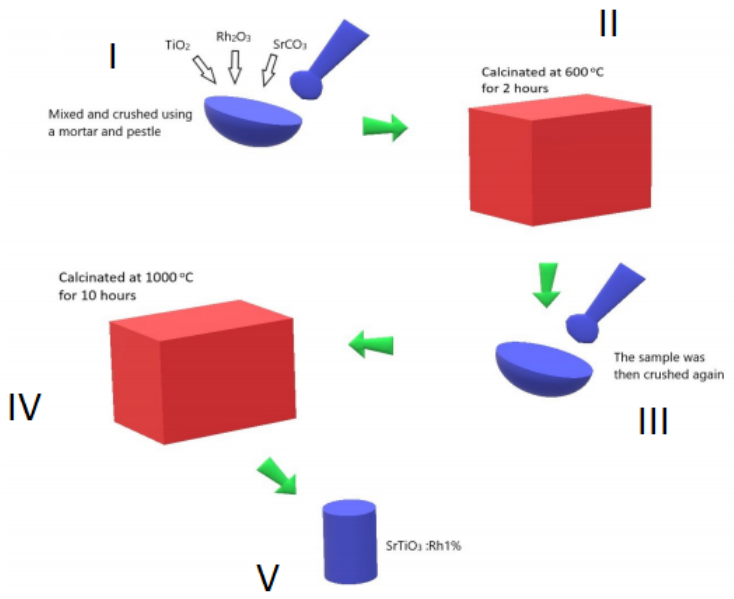

Figure 3.1: Shows a scheme of the solid state preparation method

There was made a total of 8 batches

- In Batch 1 there was made 1 gram of pure $SrTiO_3$ and 1 gram of Rh(1%) doped $SrTiO_3$. The samples were prepared separately. The samples were crushed for 30 minutes, Before and after being calcinated at 600 °C for 2 hours. After being crushed for the second time, the samples were submitted for calcination at 1000°C for 10 hours. The samples were calcinated together in static air. The samples are denoted B1 and B1.Rh for pure $SrTiO_3$ and $SrTiO_3$:Rh, respectively

- In Batch 2 there was made 2 gram of pure $SrTiO_3$. The sample was crushed for 30 minutes before and after calcination at 600 °C for 2 hours. The sample was then submitted for calcination at 1000°C for 10 hours. The sample is denoted B2

- In Batch 3 there was made 10 gram of pure $SrTiO_3$. The sample was crushed for approximately 50 minutes before and after calcination at 600 °C. The sample was then calcinated at 1000°C for 10 hours. The sample is denoted B3

- Batch 4 was calcinated in N_2 flow 100 [ml]/[min]. There was made 10 grams of pure $SrTiO_3$. The sample was crushed before, and after calcination for approximately 40 minutes. The sample was then calcinated at 1000°C for 10 hours. The sample is denoted B4

- In Batch 5 there was made 3 gram of pure $SrTiO_3$ and 3 gram (1%) Rh doped $SrTiO_3$. The samples were prepared separately. The samples were crushed for 40 minutes each, before calcination at 600 °C and after. The samples were then submitted for calcination at 1000°C for 10 hours. The samples were calcinated together. The samples are denoted B5 and B5.Rh for pure $SrTiO_3$ and $SrTiO_3$:Rh, respectively.

- In batch 6 a total of 3 grams of (2%) Rh doped $SrTiO_3$, was prepared. The sample was crushed for approximately 30 minutes and then calcinated at 1000 °C, i.e the second (II) and third (III) step in figure 3.1 was skipped. The sample is denoted B6.Rh

- In Batch 7 there was made 3 grams of rhodium doped $SrTiO_3$. The sample was crushed for approximately 50 minutes. 2-3 [ml] of methanol was added to the

mixture to create a slurry paste while crushing the sample. the sample was then submitted for calcination at 1000°C for 10 hours. The sample was prepared without the pre-calcination steps (II and III) in figure 3.1. The sample is denoted B7.Rh

- In Batch 8 there was made 2 grams of rhodium doped $SrTiO_3$. The sample was crushed for 40 minutes before calcination at 600 °C, then crushed for 40 minutes again before being submitted for calcination at 1100 °C for 10 hours. The sample is denoted B8.Rh

All calcinations were performed in a high-temperature furnace in static air except for Batch 4 which was made with N_2 flow of 100 [ml]/[min].

3.2.1 Addition of carbon quantum dots

0,65 mg of $SrTiO_3$:Rh (1%) were dispersed in a 2 ml solution containing carbon quantum dots. The solution was then submitted for drying at 60 °C for 48 hours.

3.2.2 Deposition of Pt

Pt was deposited on to the desired samples by wet impregnation. The desired amount of photocatalyst was dispersed in a Pt solution with the purpose of to achieving a 0.5% wt loading of Pt. The Pt solution, containing the dispersed photocatalytic powder was then sonicated for 30 minutes and occasionally stirred with a spatula. The sample was then submitted for drying at 120 °C overnight. The sample was then further dried in a vacuum oven for 4 hours at 60 °C. After drying, the sample was reduced in H_2 of 100 [ml]/[min] for 2 hours at 500 °C with ramp rate of 10 °C. The samples that have been loaded with Pt through wet impregnation and the reduced in H_2 are denoted with **-Pt** in the sample name and the method itself is denoted **I-R**

3.3 Characterization

Nitrogen physisorption

The Micromeritics TriStar II 3020 Surface Area and Porosity Analyzer was used for N_2 adsorption measurements. The samples were first degassed overnight, in vacuum at 200 °C. The empty tubes were weighted first and than the degassed sample was loaded into the tube. The tube was then weighted again. The tube containing the sample was then inserted into the machine and the necessary information was inserted in the software and the measurements were started. The measurements were conducted at 77K. In all cases the sample weight was approximately 60 mg.

XRF

Approximately 200 mg of photocatalyst sample were mixed with 2,5-3,0 grams boric acid and crushed, using a mortar and pestle. The sample was then placed in a hydraulic press and kept under pressure of 10 ton for about 4 minutes in order to make a pellet. The pellet was then transferred to a sample holder which was placed in the Wavelength Dispersive X-Ray Fluorescence Supermini 200 analyzer for XRF analysis.

The samples had the following mix ratio

- 201,4 mg of the top layer sample (CONT) were mixed with 2,6374 gram of boric acid
- 202,7 mg of the bulk sample (REN) were mixed with 2,6410 gram of boric acid

XRD

XRD analysis was performed with a Bruker D8 A25 DaVinci X-ray Diffractometer with Cu$K\alpha$ radiation. The samples were prepared for XRD analysis by using a method called backloading. The selected specification, for the XRD analysis, was "V6 variable slit", analyzing degrees were selected to 15-75 degrees and the analyzing time was set to 30 minutes.

UV-visible

Pellets were prepared from the desired samples for UV-visible DRS measurements. The sample was then placed in an integrating sphere, and the measurements were taken. The samples measured are listed in table 3.2.

Table 3.2: Shows the samples submitted for UV-vis DRS measurements

Sample	Rh doped in atom%	Pt loaded in wt%	calcinaton T in [°C]	Batch number	Denoted
TiO_2 P25(Sigma Aldrich)	-	-	-	-	Nr 1
$SrTiO_3$	-	-	1000	3	Nr 2
$SrTiO_3$:Rh	1	-	1100	8	Nr 3
$SrTiO_3$:Rh	1	-	1000	5	Nr 4
$SrTiO_3$:Rh-Pt	1	0,5	1000	5	Nr 5
$SrTiO_3$:Rh	2	-	1000	6	Nr 6
$SrTiO_3$-Pt	-	0,5	1000	3	Nr 7

3.3.1 Inductive coupled plasma - mass spectrophotometry

Pretreatment, about 20 mg sample was measured. 1.5 ml of concentrated ultrapure HCL and 0.5 ml of concentrated ultrapure HNO_3 was then added to the sample. The sample was then heated, in a heating cabinet, up to 105 °C until the sample was dissolved which was approximately one hour. The sample was then diluted to the appropriate concentration for ICP-MS analysis, about 230 ml. [10]

3.4 Activity measurements

3.4.1 Preparation of the solution mix

600 ml of distilled water was added to a photoreactor. 65 mg of the desired photocatalyst was then added. The mixture was then stirred with a spatula and sonicated for approximately 10 minutes. 60 ml of ethanol or methanol was then added to the mixture. If the activity test involved photodepositon of Pt, a solution containing

the desired amount of Pt would also be added to the mixture. Primarily ethanol was used. the sacrificial reagent was added to act as a *holescavenger*. The suspension was then placed in the photoreactor under stirring. Argon was used as carrier gas. Before starting the experiment, the system was purged by flowing argon gas through the system for 30 minutes. In addition the solar simulator required at least 30 minutes to stabilize before use. After 30 minutes, the solution was irradiated with light from a solar simulator with approximately 150 W effect. Sciencetech SS150 Sciencetech FRSS 1,5G filter with 1 sun condition, was the solar simulator used in the experiments. The gas exiting the reactor was analyzed, every 15 minute, with a Thermal Conductivity Detector micro gas chromotograph, Agilent Technologies 3000. Flowsheet shown in figure 3.2

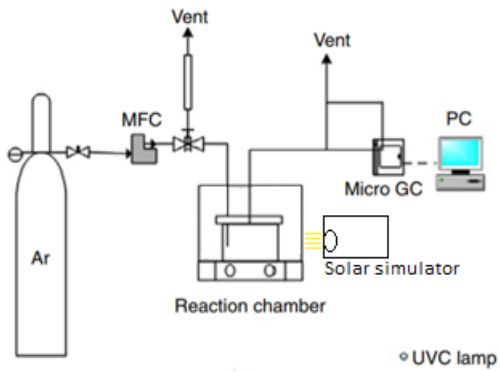

Figure 3.2: Shows a flowsheet for the photoreactor system. Reproduced and adapted from [50]

3.4.2 Photodeposition

Photodeposition (PD) was performed *In situ* by adding the desired amount of Pt solution to a solution containing 600 ml of water, 65 mg photocatalyst powder and 60 ml of sacrificial reagent. The system was then stirred for 30 minutes with a magnet stirrer, while being purged with Ar gas. After 30 minutes the solution was irradiated with the solar simulator. Samples that have been loaded with Pt by photodeposition are denoted **PD**.

3.4.3 Experimental denotations

The denotations used for describing the experiment and the sample are presented in the following list

B1 used for all synthsized samples and describes which batch the sample is from

.Rh used for samples doped with Rh.

-Pt used for samples loaded with Pt through I-R

.PD used for samples loaded with Pt through $in\ situ$ photo deposition

.MeOH used for experiments performed with methanol. If not denoted **MeOH**, the experiment was performed in ethanol.

Example for how the denotations is used can be seen in table 3.3

Table 3.3: Presents example of denotations for the performed experiments.

sample	Batch	pure or Rh doped	Pt deposition method	Sacrificial reagent
B1.Rh.1	1	Doped	-	Ethanol
B1.Rh-Pt.2	1	Doped	I-R	Ethanol
B3-Pt	3	Pure	I-R	Ethanol
B5.Rh.PD.MeOH	5	Doped	PD	Methanol
B8.Rh.PD.MeOH	8	Doped	PD	Methanol

Chapter 4

Results and discussion

4.1 Overview

An overview over the different characterization methods, performed for the different batches, is presented in table 4.1.

Table 4.1: Overview of the type of characterization applied for the different batches. Samples denoted X"Rh", where X is a number from 1-8, are doped with Rh. The asterisk indicates that the sample is submitted for analysis, but not included in the thesis.

Batch	**XRD**	**B.E.T.**	**XRF**	**ICP-MS**	**UV-vis DRS**
1	√	√	-	-	-
1.Rh	√	√	-	-	-
2	√	√	-	-	-
3	√	√	√	√	√
4	√	√	-	-	-
5	√		-	-	-
5.Rh	√	-	-	-	√
6.Rh	√	-	-	√ -	√
7.Rh	√	-	-	√	-
8.Rh	√	√	-	*	√

B8 were submitted for ICP-MS analysis, but the analysis was not finished in time to be included in the thesis

4.2 Characterization

4.2.1 XRD

XRD analysis was performed for all the prepared samples. Figure 4.1 shows the XRD-spectra of batch 1-3 including a sample of the surface layer that was observed on B3 (B3 CONT) after the calcination at 1000 °C for 10 hours. A picture of the surface layer on B3 can be seen in figure 4.3. Figure 4.2 shows the XRD spectra of batch 3 to batch 8. The XRD specter of batch 3 presented in 4.2 is the bulk sample.

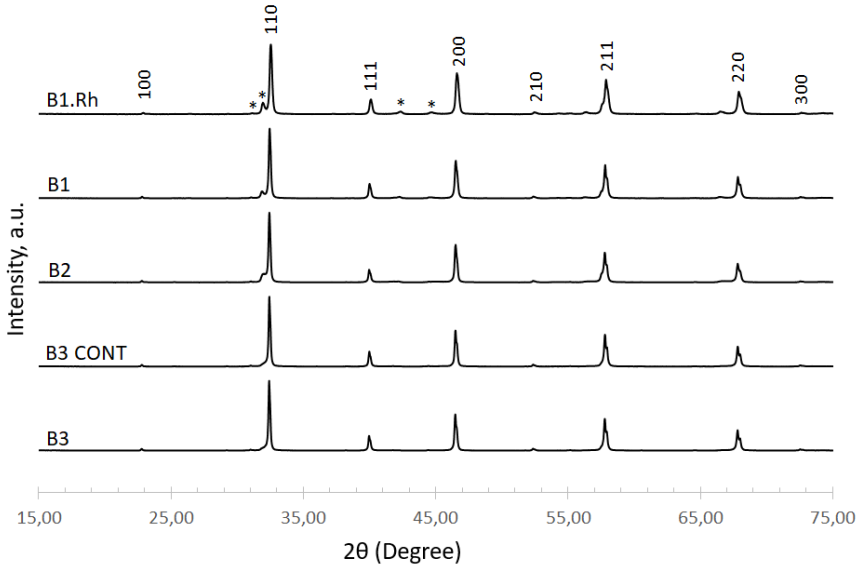

Figure 4.1: Shows the result from the XRD analysis for B1, B1.Rh, B2, B3 and the surface layer of B3 after calcination, denoted B3 CONT.

The characteristic peaks for $SrTiO_3$ are present and identified from [51]–[54]. Impurity peaks are marked with an asterisk (*). In all the samples, on the left side of the main peak, 110, there is a shoulder and to the left of the shoulder a small peak at approximately 31°. There are also two minor impurity peaks between 111 and 200 in all the samples. The shoulder and impurity peaks are present in all of the prepared $SrTiO_3$ samples. Batch 3 has the smallest impurity peaks. The doping of Rh cations up to 5 mol% should not affect the crystal structure of $SrTiO_3$ [27]. The impurity peaks are also

present in nondoped $SrTiO_3$ which further rules out the possibility of being caused by the Rh doping.

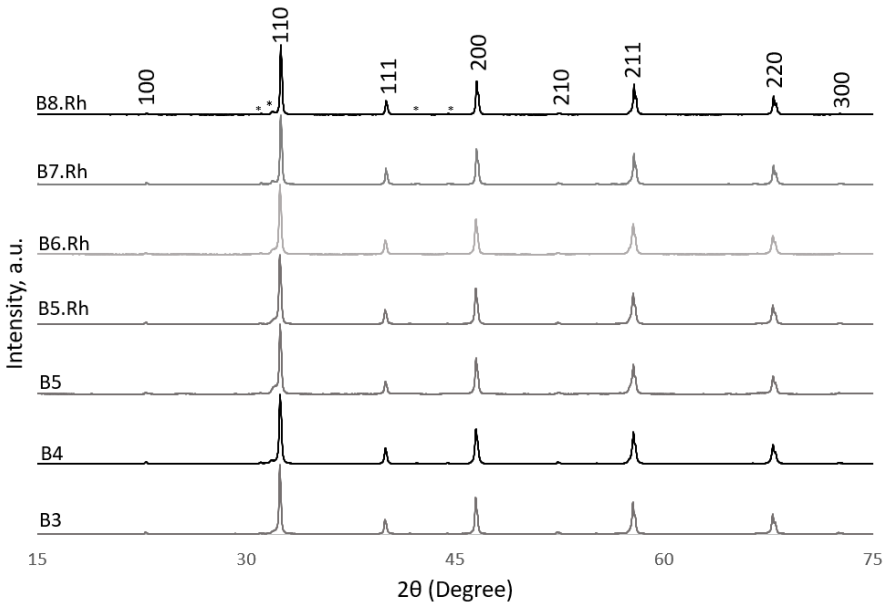

Figure 4.2: Shows the XRD spectra B3, B4, B5, B5.Rh, B6.Rh, B7.Rh and B8.Rh

In [55] a small impurity peak was found to the left of the main peak, 110, and the peak was assigned to the presence of Sr_2TiO_4. In that study the peak appeared after preparation using the solid state reaction, the calcination was performed at 900 °C. All the $SrTiO_3$ samples, in this project, were calcined at 1000 °C (or higher) for 10 hours due to this being the optimized time and temperature for the solid state reaction for $SrTiO_3$:Rh [8]. The impurity peaks were also attempted identified by using the XRD analysis software. Figure B.15 in Appendix B shows a possible presence of $Sr_3Ti_2O_7$, but it is not possible to conclude the presence of the substance based solely on the match finding in the analysis software.

Figure 4.3: shows a picture taken of B3 after being calcined in the high-temperature furnace. Observe the color of the top layer.

XRD analysis was not performed for the metal loaded samples as metal loading of 0,5 wt% is not expected to be detectable in the XRD analysis. To further investigate the impurity peaks, the precursor compounds, $SrCO_3$ and TiO_2 (P25), were submitted for XRD analysis along with a sample from the precursor mixture for Batch 4. The sample was taken after the second step in the preparation method shown in figure 3.1. The comparison of the XRD spectra can be seen in figure 4.4. HW B4 represents the sample of the precursor compound after the first calcination at 600 °C. HW B4 looks very similar to $SrCO_3$ apart from a peak at 2θ = 32,4°. Apart from the main peak which coincides with the main peak of $SrTiO_3$, the peaks from the TiO_2 spectra seem to vanish after the first round of calcination.

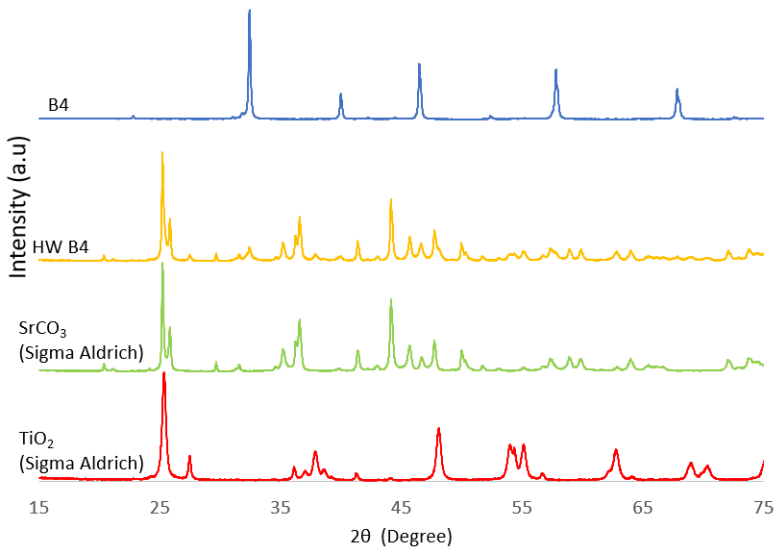

Figure 4.4: Shows the XRD spectra of the precursor compounds, TiO_2 (P25) and $SrCO_3$ for $SrTiO_3$, purchased from Sigma Aldric. B4 is $SrTiO_3$ from Batch 4, B4HW is the mixed precursors after calcination at 600 °C for 2 hours

From batch 1 up to batch 3 the impurity peaks appear to become smaller. The sample in batch 3 was grinded for about 50 minutes due to the amount of sample being more substantial than the previous samples made. As 40 minutes of grinding was deemed sufficient the batch 4 received around 40 minutes in grinding time between the first calcination. Due to the top brown/yellow layer on the batch 3 sample, 4.3, batch 4 was calcined in a glass reactor using N_2 flow to see if that could improve preparation. During the calcination, the thermometer, inside the reactor showed a temperature of only 950 °C.

The impurity peaks were more present in batch 4 than in batch 3. There can be several reasons. The first reason being, the temperature had stagnated at 950°C inside the reactor. Second, a small amount of the precursor compound was taken for XRD measurements. If precursor compound is not entirely homogeneous and a small amount is removed, the stoichiometry in the product can be influenced. The third being that the sample was calcined in N_2 flow instead of static air. Though many factors could have contributed to the increased presence of the impurity peaks, calcination in

N_2 flow was abandoned.

The impurity peaks are present again in B5 and B5.Rh. Due to this, the synthesis method was reviewed again. Calcinating the precursor compound for 2 hours and then grind it again should facilitate the sample better [23], but as the impurity peaks still were present, the approach was altered in B6.Rh. In B6.Rh, step II and III, from figure 3.1, were skipped as these steps are not mentioned in [8] and [10], [24], [56], refers to the synthesis method in [8] as the synthesis for preparing $SrTiO_3$ and $SrTiO_3$:Rh. The method described in [8] requires the $SrCO_3$ to be calcined at 300°C prior to usage. The B6.Rh sample was grinded for 30 minutes. In figure 4.5 the XRD spectra of $SrCO_3$ and $SrCO_3$ after calcination at 300°C for 1 hour. No differences could be observed in the comparison of untreated $SrCO_3$ XRD spectra and the treated $SrCO_3$ spectra.

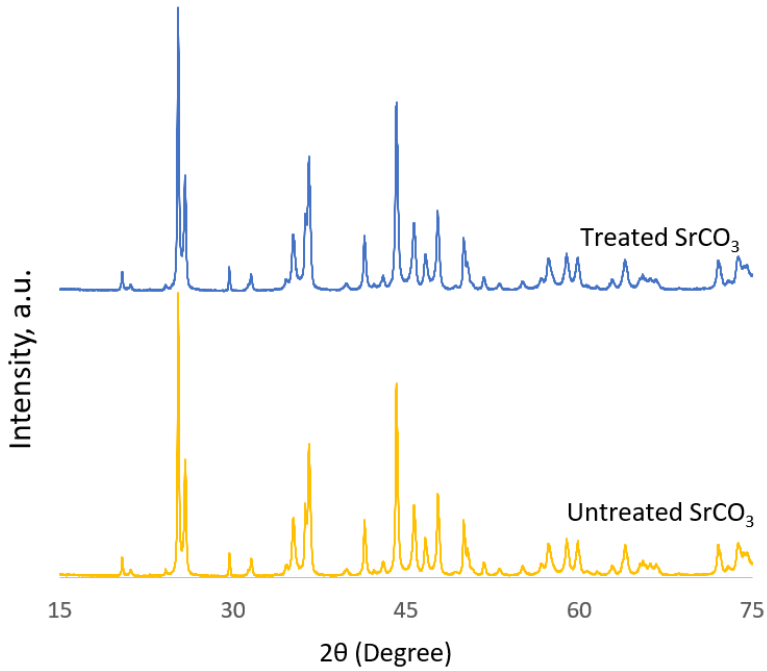

Figure 4.5: XRD spectre of $SrCO_3$ before and after calcination at 300 °C for 2 hours

The impurity peaks were also present in B6.Rh and it was decided to try the same preparation method again with longer grinding time and the addition of methanol, to further facilitate mixing of the sample [57]. B7.Rh was then prepared, with focus on

grinding and mixing of the sample, but the impurity peaks remained.

The thermometer on the high-temperature furnace was showing 1000°C during the calcination, but there was no thermometer measuring the temperature directly on the sample container. To ensure that the sample was calcined at a high enough temperature, a new batch was made with a calcination temperature of 1100°C. Figure 4.6 shows a picture of the powder made in B7.Rh, figure (a), and the powder made in B8.Rh, figure (b). The color of the powder made in B7.Rh matches all of the previously made batches of Rh doped $SrTiO_3$, but the color in B8.Rh is clearly darker with a purple hint.

(a) Shows the color of the B7.Rh powder (b) Shows the color of the B8.Rh powder

Figure 4.6: Shows the color difference between the Rh doped $SrTiO_3$ calcinated

However, regardless of the color change, the impurity peaks remain in the XRD spectra for B8.Rh as well.

4.2.2 XRF

As no differences between the top layer and the bulk sample from batch 3, the samples were submitted for further investigation through XRF analysis. The results can be seen in table 4.2

Table 4.2: Shows the results from the XRF analysis of the top layer and bulk sample of batch 3 $SrTiO_3$

Substance	**B3 bulk** **wt %**	**B3 Top layer** **wt %**
SrO	55,30	53,86
TiO_2	43,75	44,75
Al_2O_3	0,44	-
K_2O	0,52	0,34
SiO_2	-	0,26
Cl	-	0,02
Fe_2O_3	-	0,11
Ag_2O	-	0,66

As can be seen from 4.2, There are a lot more substances present in the top layer sample. The expected substances in both samples, SrO, and TiO_2, amounts to 99,05 wt% and 98,6 wt% for the bulk sample and the top layer sample, respectively. The difference between the amount of the expected substances is ~ to 0,4 wt%.

Preparation of the XRF samples is very delicate and has to be performed in precisely the same way if samples are to be compared. There is also a risk of the sample being exposed to contamination during the preparation. If the preparation method is not performed properly or the sample has been contaminated during the preparation, the results will be less accurate.

The results show more contamination for the top layer sample which is in accordance with the expectations prior to the analysis, but the difference of contamination in the two samples are less than expected.

4.2.3 N_2 Physisorption

The samples submitted for N_2 physisorption measurements along with the corresponding BET surface area can be seen in table 4.3.

Table 4.3: Shows the BET surface area for the samples submitted for N_2 physisorption measurements

Sample	**B.E.T. Surface area** $[m^2/\text{g}]$
B1	6,0
B1.Rh	7,1
B2	6,6
B3	7,8
B3-Pt	6,4
B4	7,7
B8.Rh	2,9
TiO_2 P25 (Sigma Aldrich)	48,8

The BET result is showing a much lower surface area for $SrTiO_3$ than for TiO_2 this is likely due to sintering caused by the high calcination temperature, 1000 °C. The measured surface area is within the expected range, 4-12 $\frac{m^2}{g}$ [23], [58]–[60]. Metal loading was not expected to influence the surface area significantly [50]. To verify this, the B3-Pt was submitted for N_2 physisorption. All of the samples calcined at 1000 °C show a result between 6 and 7,8 $\frac{M^2}{g}$. It is possible that the variation in the surface area for the samples calcined at 1000 °C is due to experimental error. Because the B8.Rh was calcined at 1100 °C it was expected to have a lower surface area [60].

$SrTiO_3$ is a very stable photocatalyst and resistant to photocorrosion [61]. The surface area is therefore not expected to change during the photoreaction. The N_2 physisorption measurements require a minimum of 50 mg of photocatalyst to measure the surface area. As the experiments are carried out with 65 mg dissolved in 660 ml solution, retrieving more than 50 mg becomes a delicate process.

4.2.4 UV-visible spectrophotometry

UV-visible DRS was applied to obtain the absorbance spectra and to find the band gap for the, differently, synthesized samples of $SrTiO_3$ and $SrTiO_3$:Rh. The absorbance spectra can be seen in figure 4.7. The samples submitted for the measurements are TiO_2 P25 (Sigma Aldrich) = 1, B3 = 2, B8.Rh = 3, 4 = B5.Rh, 5 = B5.Rh-Pt, 6 = B6.Rh and 7 = B3-Pt.

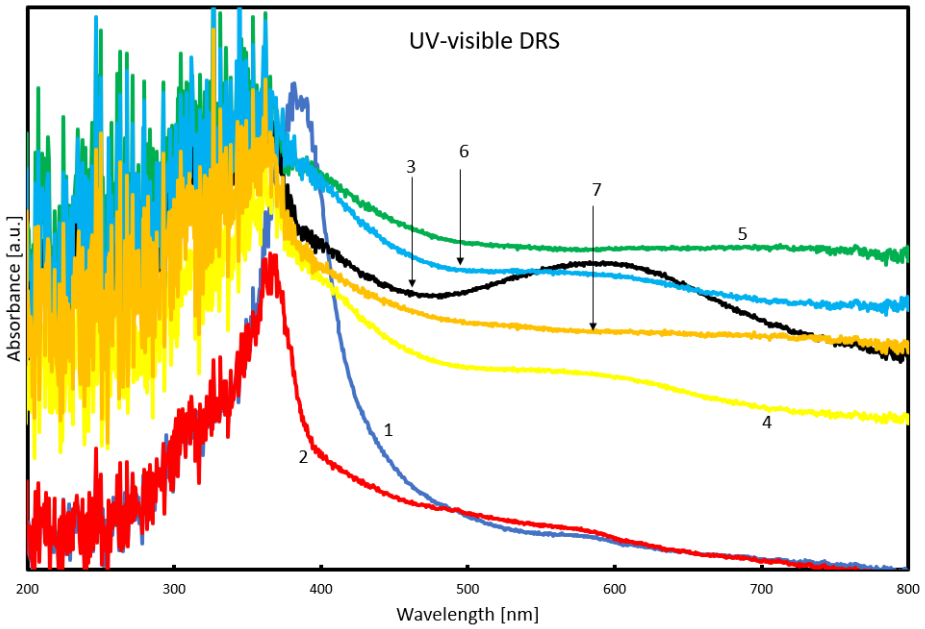

Figure 4.7: Shows the absorbance spectra for differently prepared samples of $SrTiO_3$ and Rh doped $SrTiO_3$. 1 = TiO_2 P25, 2 = B3, 3 = B8.Rh, 4 = B5.Rh, 5 = B5.Rh-Pt, 6 = B6.Rh and 7 = B3-Pt

From figure 4.7 it can be seen that $SrTiO_3$ shows an absorption edge at approximately 385 nm which is in accordance with literature [8], [62], [63].The TiO_2 P25 is also, as expected, in accordance with literature [64]. The absorbance spectra of the $SrTiO_3$ powders doped with Rh have shoulders into the visible light region. The shoulders can indicate that the Rh has formed a discontinuous level in the forbidden band [8]. In addition to the shoulder into the visible light region, it can be seen that B8.Rh has a broad absorption band around 580 nm, this has also been observed in [8]. [8] also observed an absorption band around 1000 nm, which also is present in B8.Rh and can be seen in figure C.1 in appendix C. The broadband peaks can indicate that some doping levels were formed in the forbidden band due to different oxidation levels[8]. It is also stated in [8], that the DRS spectra for $SrTiO_3$ loaded (not doped) with Rh or Rh oxides by an impregnation method are different from the spectra obtained for B8.Rh. For the two other Rh doped samples, the absorbance around 580 is not as clear as it is for B8.Rh. There can be observed a small "bump" for B5.Rh in figure 4.7. For B6.Rh it

is questionable if the peak is present, but from the data set used for drawing the plot, a small increase in absorbance is observed. For the samples loaded with Pt, a change in the absorbance spectra can be observed.

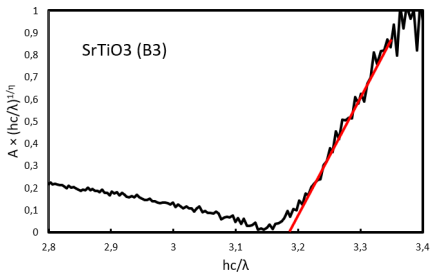

(a) shows the extrapolation to find the band gap for $SrTiO_3$

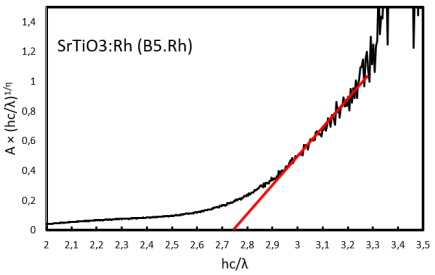

(b) shows the extrapolation to find the band gap for B5.Rh

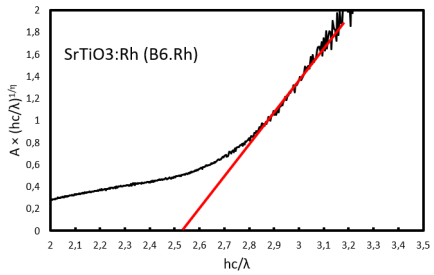

(c) shows the extrapolation to find the band gap for B6.Rh

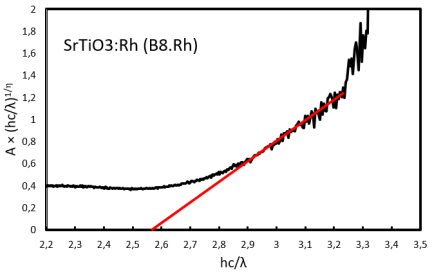

(d) shows the extrapolation to find the band gap for B8.Rh

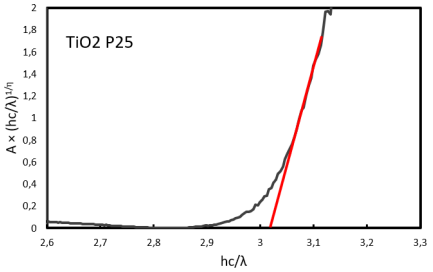

(e) shows the extrapolation to find the band gap for TiO_2 P25 (Sigma Aldrich)

Figure 4.8: shows the extrapolation to find the band gap for $SrTiO_3$.

As stated in the theory chapter, The band gap can be found through the Kebulka-Munk method. The extrapolation to find the band gap for the different substances can be viewed in figure 4.8. (a) is for $SrTiO_3$ (B3), (b) is for $SrTiO_3$:Rh (1%) (B5.Rh), (c) is for $SrTiO_3$:Rh (2%) (B6.Rh), (d) is for $SrTiO_3$:Rh (1%) (B8.Rh) and (e) is for TiO_2 P25 (Sigma

Aldrich). The accuracy in the Kubelka–Munk is stated to be sufficient for band gap measurements in photocatalysis [65].

The y-axis in figure 4.8 is found from A × $(\frac{hc}{\lambda})^{\frac{1}{\eta}}$. η is dependent on the type of band gap transition. For a direct allowed band gap transition η is equal to 0,5. For an indirect allowed band gap, η is equal to 2. For an indirect and direct forbidden transition, η is equal to 3 and $\frac{3}{2}$, respectively.[65]

Different values of η were explored for all samples. The best value of η for TiO_2 P25 was found to be 0,5 which gives a band gap of 3,0 [eV] which in turn is consistent with literature [6]. The other values of η gave band gap in the range of 2,8-2,7 [eV] and were, therefore, discarded. For $SrTiO_3$ literature stated that the majority of reports agree that $SrTiO_3$ has an indirect band gap, η = 2 [66], [67]. This gives a band gap of 3,2 [eV] and is consistent with literature [6].

For the Rh doped $SrTiO_3$:Rh samples the only value of η that gave a sensible band gap was 0,5, direct band gap. The band gap for B5.Rh, B6.Rh and B8.Rh was found to be 2,7 [eV], 2,5 [eV] and 2,6 [eV], respectively. This shows that the Rh has narrowed the band gap, but the band gap found in literature for $SrTiO_3$:Rh (1%) is 2,3 [eV] [8], [9].

The samples with the obtained band gap and the corresponding η is listed in table 4.4

Sample	Measured band gap [eV]	η band gap transition factor
TiO2 P25	3,0	0,5
B3	3,2	2
B5.Rh	2,7	0,5
B6.Rh	2,5	0,5
B8.Rh	2,6	0,5

Table 4.4: Contains the obtained band gap and the η value for the samples submitted for absorbance spectra measurements

4.2.5 ICP-MS

The stoichiometric amount of Sr has been shown to be of major importance for the photocatalytic activity of $SrTiO_3$ [68]. In [10] it was shown that $SrTiO_3$:Rh (1%), synthesized with the Solid state method, with ratio = Sr/Ti 1.02 had a H_2 evolution that

was 3 times higher than the sample with ratio Sr/Ti = 1.0 [10].

Because the stoichiometric amount has such a tremendous amount of influence on the photocatalytic H_2 evolution, some samples were submitted for ICP-MS analysis to investigate the mole ratios between Sr and Ti+ Rh. The results from the samples submitted for ICP-MS analysis can be viewed in table 4.5.

Table 4.5: Shows the wt% and the ratio between Sr and Ti + Rh for the samples submitted for ICP-MS analysis. The row named "Intended", shows the intended value of Sr, Ti and Rh for each sample along with the mole ratio.

Sample	Sr (wt%)	Ti (wt%)	Rh (wt%)	Sr/(Ti+Rh) mole ratio	Pt (wt%)
Intended	48,1	25,5	0,554	1,02	
B1.Rh-Pt	47,2	23,86	0,33	1,07	0,83
B3	43,4	22,9	-	1,04	-
B3-Pt	44,7	21,62	-	1,13	0,77
B4	48,3	19,1	-	1,39	-
B4-Pt	45,5	25,3	-	0,98	0,87
B5-Pt	45,0	23,2	-	1,06	0,91
B5.Rh-Pt	45,0	21,9	0,29	1,12	0,9

All the samples were made with the intention of having a Sr/Ti ratio = 1,02. If the sample were doped with Rh, the ratio would be Sr/(Ti+Rh) = 1,02. From the ICP-MS results, displayed in table 4.5, the ratio in several of the samples is far from the intended ratio.

The pure sample of batch 3 is showing a ratio of 1,04. However The same sample, only loaded with Pt through wet impregnation, is showing a ratio of 1,13. Because the sample has first been exposed to wet impregnation and then reduction, the sample, at some point could have been contaminated leading to a disturbance in the ratio. Pt is not suspected of interfering with the signal of Sr, Ti or Rh. The reason for the different ratios, considered most probable, is that the sample is not homogeneous and therefore some differences in the ratio can occur. The pure sample of batch 4, is as far of as having a Sr/Ti ratio = 1,385. Considering the XRD spectra of B3 and B4 along with the ICP-MS results, it seems reasonable to assume that the B3 is more homogeneous than B4.

The Pt loading in all samples was above 0,5 wt % in all the Pt loaded samples. A possible explanation for this is that the Pt is not adequately dispersed on to the photocatalyst

and, by chance, contained more Pt. Because all of the samples loaded with Pt contains approximately the same amount of Pt, 0,8 ~ 0,9, a more likely reason is that the Pt precursor contained more Pt then what was accounted for.

There are some insecurities in the results. The original results showed a presence of Ca of between 20 and 25 wt% in each sample. After investigating the Ca signal, it was attributed to Sr^{2+} and was it was decided that the Ca values should be removed entirely from the results. The detected wt% after removing the Ca values are displayed in table 4.6. In regards to the low signal of Rh. It was known that the Sr signal would interfere with the signal obtained from Rh and an attempt to compensate was made. However, the low Rh is likely caused by interference from Sr.

The missing mass percentage is assumed to be oxygen. The estimated wt% can be seen in table 4.6.

Table 4.6: Shows the wt% and the ratio between Sr and Ti + Rh for the samples submitted for ICP-MS analysis. The row named "Intended", shows the intended value of Sr, Ti and Rh for each sample along with the mole ratio.

Sample	(wt%) found	Assumed O (wt%)
B1.Rh-Pt	72	27,8
B3	66	33,7
B3-Pt	67	32,9
B4	67	32,6
B4-Pt	72	28,3
B5-Pt	69	30,9
B5.Rh-Pt	68	32,0

There were detected small amounts of impurities, the most abundant being Fe with a signal ~ 0,04 wt%. As finding impurities was not the objective of the analysis, not all elements were included in the ICP-MS analysis. The foreign elements that obtained the most significant values are listed in table 4.7

Table 4.7: Shows the wt% and the ratio between Sr and Ti + Rh for the samples submitted for ICP-MS analysis. The row named "Intended", shows the intended value of Sr, Ti and Rh for each sample along with the mole ratio.

Sample	Al (wt%)	Cr (wt%)	Fe (wt%)
B1.Rh-Pt	0,01	0,002	0,009
B3	0,002	0,009	0,03
B3-Pt	0,003	0,009	0,036
B4	0,002	0,001	0,006
B4-Pt	0,002	0,003	0,017
B5-Pt	0,003	0,007	0,028
B5.Rh-Pt	0,02	0,01	0,042

The B5.Rh-Pt has the largest amounts of impurities, but the values in general are low, <0,05 wt%.

Comparing the ICP-MS results for B3 with the B3 bulk sample from the XRF analysis, the XRF analysis, it can be seen that both Al and Fe are present in both analysis though the XRF reported it to be Al_2O_3 and Fe_2O_3, and

4.3 Experimental setup

In [6] it is stated that the amount of photocatalyst should be optimized for each experimental setup and that the photocatalytic activity is dependent on the number of photons absorbed by a photocatalyst unless the light intensity is too strong.

The amount of photocatalyst used for the photocatalytic experiments with the solar simulator was set to 65 [mg]. The amount was selected by suspending different amounts of photocatalytic powder with same amounts of water and sacrificial reagents used in the experiments, then irradiate the solution and observe if the solution absorbs all the light. From the observation, amounts less 65 [mg] also seemed to absorb all the light from the solar simulator, but to ensure all the light was absorbed by the photocatalytic solution, it was decided to proceed with 65 [mg]. In figure E.3 in Appendix E, a picture of the irradiated photocatalytic solution can be seen to absorb all the light. Ideally, activity measurements should have been performed to verify the optimal amount for the experimental setup. Because the primary objective in the

thesis was to investigate the effects of CQD's on the photocatalytic performance of rhodium doped $SrTiO_3$, finding the optimized amount for the setup would not impact the main investigation and was, therefore, out of scope. [6]

Due to the photocatalytic activity, usually, not being proportional to the weight of the photocatalyst, [6] states that normalization of the photocatalytic activity by weight is not acceptable.

Apparent quantum yield

If the experimental conditions, e.g., light source or reaction cell, are not the same, the photocatalytic activity cannot be compared because the reaction conditions are different. Determining the quantum yield, therefore, becomes important. However, Determining the real amount of photons absorbed by the photocatalyst is a tough procedure and the quantum yield, obtained in this project, is, therefore, an apparent quantum yield (AQY). Usually, the number of absorbed photons is lower than that of the incident light; the apparent quantum yield is therefore estimated to be smaller than the real quantum yield. [6]

The AQY can be found from equation 4.1. How to find the number of reacted electrons and the total number of photons absorbed can be seen in Appendix D in equation D.1, D.2, D.3 and, D.4. [69]–[72]

$$\text{AQY} = \frac{\text{Number of reacted electrons}}{\text{Total number of photons absorbed}} \tag{4.1}$$

4.4 Activity measurements

No H_2 evolution could be detected for the synthesized samples, submitted for activity testing without a co-catalyst, even though a sacrificial reagent is present. The only sample evolving H_2 without a co-catalyst was the TiO_2 P25 from Sigma Aldrich. There can be several reasons for the TiO_2 P25 showing activity, the two most obvious being that the BET results showed a surface area approximately 7 × larger than the

synthesized sample and the other being that it is purchased from Sigma Aldrich with high quality and purity.

Pt was the only co-catalyst used in the experiments. Pt was used due to the metal being highly conductive and known to have a good performance. The cocatalyst is added to provide active sites. If the active sites for redox reactions do not exist on the surface, the electrons and holes have to recombine with each other [6].

Figure 4.9 shows a comparison between $SrTiO_3$ and Rh doped $SrTiO_3$, impregnated with Pt by wet impregnation and then thermally reduced in a H_2 flow. Both of the samples appear to start producing H_2 immediately. The B3-Pt is showing a lot more photocatalytic activity than the B1.Rh-Pt.

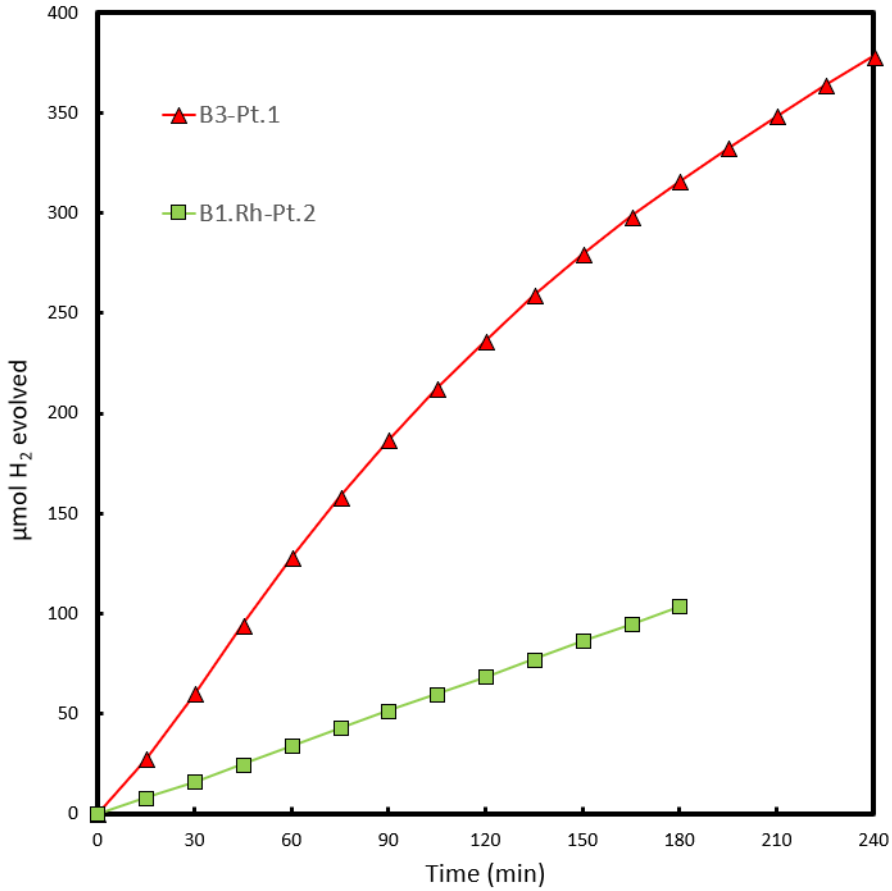

Figure 4.9: Shows the H_2 evolution from $SrTiO_3$ and Rh doped $SrTiO_3$ with I-R deposited Pt

From figure 4.9, it can be seen that the undoped $SrTiO_3$ is exhibiting a much higher photocatalytic activity than the Rh doped $SrTiO_3$. This behavior was unexpected as the Rh doping should improve the photocatalytic activity of $SrTiO_3$ because it narrows the band gap, becoming active in the visible light region [8]. Considering the BET surface area for the two samples is relatively similar and that the band gap is found to be narrower other explanations must be considered.

In table 4.8 the calculated APQ along with the experiment duration, induction time and the evolved H_2 per hour, is listed. Both the APQ and the evolved H_2 per hour are linear approaches, and from 4.9 it can be seen that the B3-Pt is not linear and that activity

decreases with time. The reason for the decrease in activity from B3-Pt is not known. To investigate if the sample was being oxidized, $SrTiO_3$ was submitted for thermal reduction, without being loaded with Pt, and then submitted for photocatalytic activity measurement. As mentioned earlier, none of the synthesized samples submitted for activity measurement produced any detectable amount of H_2 and this was the case for the reduced samples as well. If the sample indeed was being oxidized, is not uncovered, but another suggestion for the decreasing of activity is that the Pt is leaching from the photocatalyst during the photoreaction. Other reaction paths have not been considered.

Table 4.8: Shows the experimental results for the thermally reduced samples

Experiment	Experiment duration [h]	induction time	$[\frac{\mu mole H_2}{hour}]$	APQ (%)
B3-Pt.1	4	0	94,6	0,45
B1.Rh-Pt.2	3	0	34,5	0,15

The comparison with thermally reduced Pt loaded samples was performed at an early stage in the project, the sample doped with 2% Rh and the sample calcined at 1100 °C had not been made at the time. As mentioned in the theory chapter, photodeposition yields a high dispersion of the metal, only in the elemental state, and subsequently, the rate of H_2 evolution is higher than samples prepared by impregnation [32] [33]. This was also confirmed in [8]. Because of this, the primary focus was to load Pt on to the photocatalyst by photodeposition and comparing the last two samples was, therefore, left out.

Figure 4.10 shows the hydrogen evolution from the synthesized samples with $In\ situ$ photodeposition of Pt.

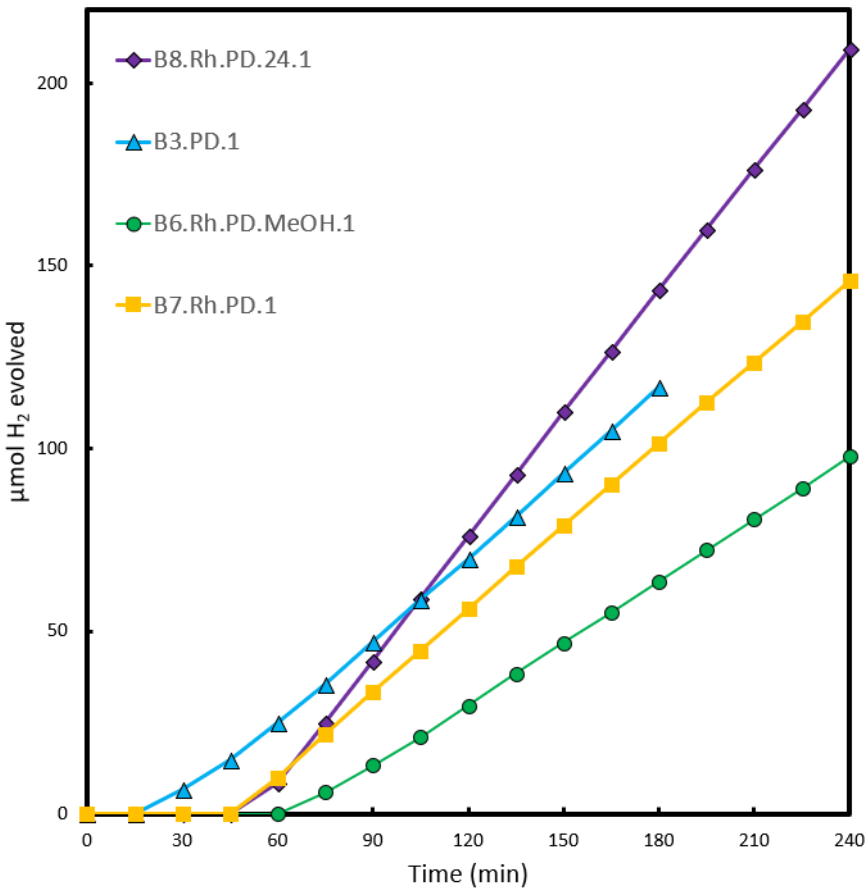

Figure 4.10: Shows the experimental results for the samples with *in situ* photodeposition of Pt

From the plot, it can be seen that the B8.Rh sample yields the highest H_2 evolution. As the B7.Rh sample was doped with 1% Rh and calcined at 1000 °C, which is the most optimal doping amount and calcination temperature [8], it should have been the most active photocatalyst of the compared samples. However, it is barely evolving any more H_2 than the pure $SrTiO_3$, and because the quantum yield is dependent on the band gap, the APQ for the B7.Rh.PD.1 becomes lower than for the B3.PD.1. The results from the activity measurements shown in figure 4.10 are listed in table 4.9.

Table 4.9: Shows the experimental results for the samples with photodeposited Pt

Experiment	Experiment duration [h]	induction time	$[\frac{\mu mole H_2}{hour}]$	APQ (%)
B3.PD.1	3	15	42,5	0,20
B6.Rh.PD.MeOH.1	4	60	32,6	0,13
B7.Rh.PD.1	4	45	44,9	0,19
B8.Rh.PD.24.1	24	45	65,1	0,27
TiO_2-P25.PD	24	0	274,2	1,24

The least active sample with photodeposition was the $SrTiO_3$:Rh (2%). The best sample was B8.Rh.PD.24.1 despite having the lowest surface area of all the samples. [6] states that a high crystallinity is often required rather than a high surface area due to recombination between photogenerated electrons. When comparing the XRD spectra of B7.Rh and B8.Rh, found in Appendix B, figure B.10 and B.11, the specters look equally crystalline. However when comparing the UV-vis specters, the B8.Rh is more in accordance with literature. Figure 4.13(c) shows a picture of the photocatalytic solution when the B8.Rh was dispersed, prior to irradiation. Figure 4.13(b) shows a picture of the color of the solution after 4 [hour] irradiation from the solar simulator. The color change from grey/purple to yellow is very conspicuous and was also reported in [8]. The change in color is thought to be caused by the Rh ions with different oxidation states getting reduced by the photogenerated electrons, as described in the theory chapter for the proposed mechanism. [8] reports changes to the absorption spectra after the photoreaction. The peak that was measured around 580 nm had vanished, and the shoulder around 420 nm had increased. It was desirable to perform a DRS measurement of the B8.Rh after the photoreaction to verify the same changes, but the amount of salvaged photocatalyst was too small for measurement. A change in color of the solution for the other samples of Rh doped $SrTiO_3$, calcined at 1000 °C was not noticed.

A photocatalytic activity test was also performed for TiO_2 P25 (Sigma Aldrich) with $in\ situ$ photodeposition of Pt. The result can be seen in figure 4.11. The rate at which it produces H_2 is much higher than the differently synthesized samples of $SrTiO_3$. Because Pt is added as a precursor salt, photoreduction is needed for the Pt to deposit. The increasing slope for the TiO_2 is believed to be the Pt depositing on

to the surface and introducing more active sites along the way. The induction time might also be an indication of the photoreduction efficiency. After 4 hours into the photoreaction, the slope of the TiO_2 P25 is producing H_2 at an even higher rate than the B3-Pt did at the start before the slope started to decrease. It must be noted that the Pt loading is uncertain after photodeposition and that different Pt loading can affect the performance of the photocatalyst.

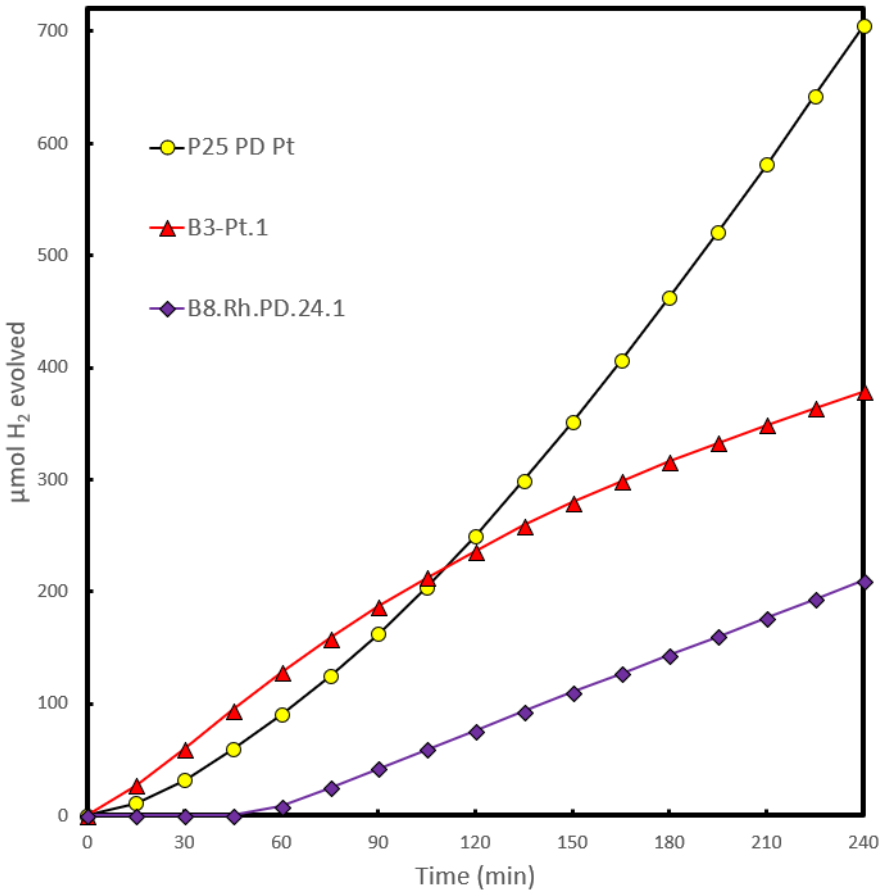

Figure 4.11: Shows H_2 evolution for B3-Pt.1, B8.Rh.PD.24.1 and TiO_2 over 4 hours

Figure 4.12 Shows the full length of the experiments performed for the TiO_2 P25 and the B8.Rh.PD.24.1. From the plot it can be seen that the H_2 evolution proceeds steadily on both photocatalysts.

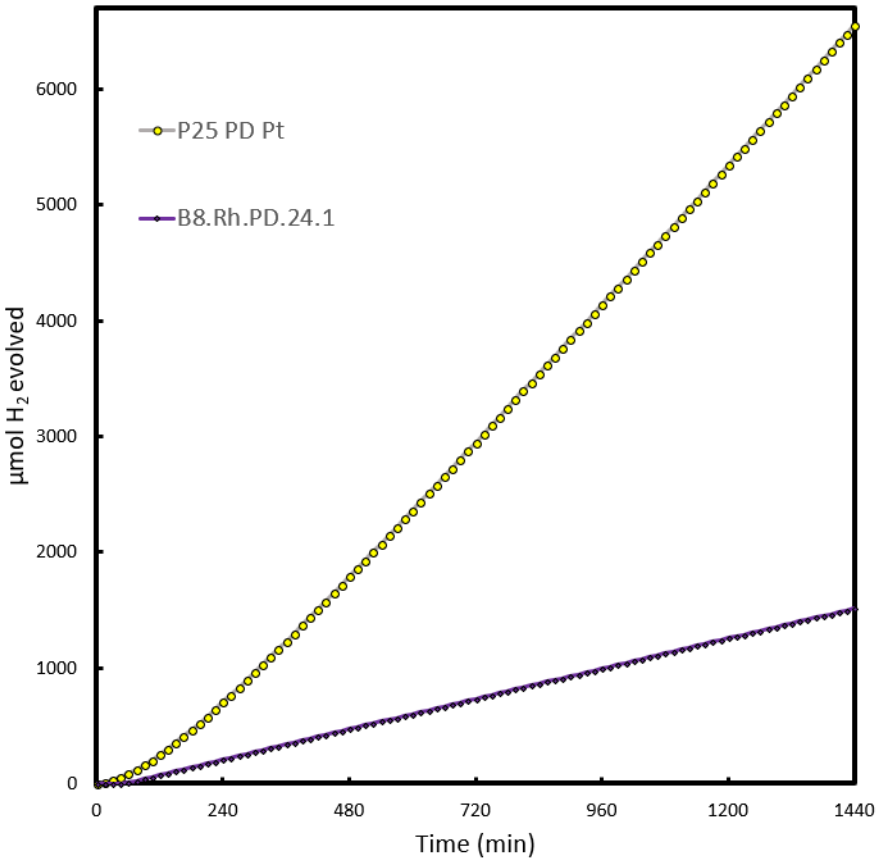

Figure 4.12: Shows the H_2 evolution over B8.Rh and TiO_2

The experimental time was increased so that it would be easier to detect deviation and verify that the H_2 was evolving at a stable rate. Because of the decrease in H_2 evolution over the B3-Pt being so significant during the 4 hour experiment, and the B8.Rh produced H_2 with the highest rate of the synthesized samples with photodeposited Pt. In addition, the steady evolution of H_2 was confirmed with performing the 24 hour experiment, the B8.Rh is considered to be the most active photocatalyst of the synthesized samples.

Except for the band gap being wider, 2,6 vs. 2,3 eV, the B8.Rh exhibits all the characteristics similar to those found in literature [8]. It is, therefore, believed that the synthesis of Rh doped $SrTiO_3$ has been successful in B8.Rh. The reason for TiO_2

P25 being more active than B8.Rh might be explained by the XRD specter. As there are found impurity peaks in the XRD specter, it is possible that these impurity peaks promotes recombination of electrons and holes in the sample, making it less active. Then there is also the surface area being measured to 2,9 $\frac{m^2}{g}$ vs. 48,8 $\frac{m^2}{g}$ which also affects the photocatalytic activity.

The scope of this project was to enhance the photocatalytic activity of the Rh doped $SrTiO_3$; therefore, it was decided to proceed with the B8.Rh and depositing CQD's on the photocatalyst to see if they could enhance the photocatalytic activity. Arguably, they could have been loaded on to the TiO_2 for investigation. However, the CQD's completely hampered the photocatalytic activity of the B8.Rh. There were performed two 24 hour experiments with the loaded CQD's. The reason for the hampered photocatalytic activity is believed to be caused by a polymer in the precursor for the CQD's. More about the CQD's experiments can be found in Appendix E. The CQD's need to be investigated further.

4.4.1 The synthesis

In this project, the only synthesis method used was the solid state. The same impurity peaks were found, at a different intensity in all of the samples XRD spectra. Due to the impurity peaks and the TiO_2 P25 being vastly more active than the synthesized samples, the synthesis method via solid state reaction should be reviewed to see if it can be improved. One suggestion on how to improve the synthesis is to synthesize the exact amount that will be used in one photoreaction. By doing this, the stoichiometry will be preserved along with the Sr/(Ti+Rh) ratio. Also, other synthesis methods such as the sol-gel and the hydrothermal method, both mentioned briefly in the theory section, should be performed and compared in photocatalytic activity.

4.4.2 Impregnation method

The pore volume of the synthesized $SrTiO_3$ was found to be 0,34 $\frac{ml}{g}$ by dripping water on to the powder until it reached saturation. However, due to the small pore volume,

dispersing the precursor solution to the entire photocatalyst surface without exceeding the saturation point proved difficult. Wet impregnation was therefore performed instead.

4.4.3 Sacrificial reagents

In some of the experiments, methanol was used instead of ethanol. The purpose was to investigate if there could be observed a difference in H_2 evolution, from a methanol solution versus ethanol solution. As reproduce-ability of the experiments was already a challenge, and the preliminary activity results with methanol seemed reasonably similar to the activity results with ethanol. Besides with this being out of the scope for the project and the difference of H_2 evolution for the two different sacrificial reagents have already been reported to be similar [73], this investigation was not pursued. Since ethanol was the sacrificial reagent that had been used the most, it was decided to continue the activity experiments with ethanol as the sacrificial reagent. The activity measurements carried out in methanol is marked with MeOH. Some of the preliminary results from the ethanol-methanol comparison can be seen in Appendix E ref.

4.4.4 pH in photocatalysis

Due to the importance of pH in the solution, the pH was measured with an indicator. The expected pH was 7, as it was distilled water that was being used, but the indication was around pH 5. The distilled water was then tested, and it was then discovered that the pH in the pure distilled water was 5. Due to this unexpected source of error, some additional activity measurements were performed with untreated water (tap water) due to the pH being measured to approximately 7. From the experiments conducted with tap water a much longer induction time was observed and though the GC measurements are showing H_2 evolution, the color of the solution is still dark grey-ish as can be seen from picture 4.13. The H_2 evolution was much lower for the experiments performed in tap water than in distilled water. The experiments with tap water were carried out for 4 hours. Picture 4.13 shows the same experiment executed with distilled water and the color of the solution is light yellow, indicating that the Rh

is reduced to Rh^{3+} [8]. Due to the lack of color change, it can be assumed that the induction period for the experiment performed 4.13 is not finished.

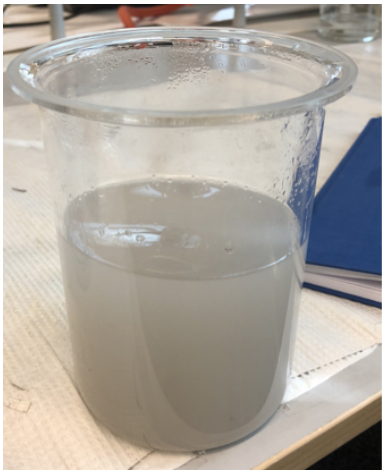

(a) Shows the color of the solution, with tap water, after 4 hours of irradiation from the solar simulator

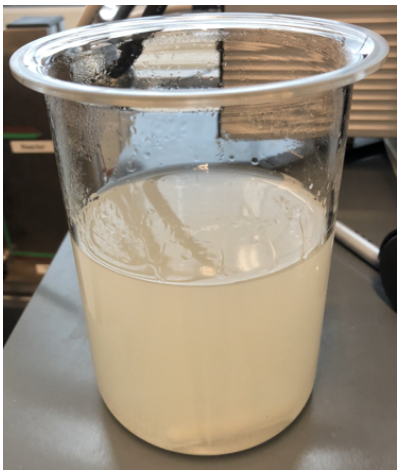

(b) Shows the color of the solution, with destilled water, after 4 hours of irradiation from the solar simulator

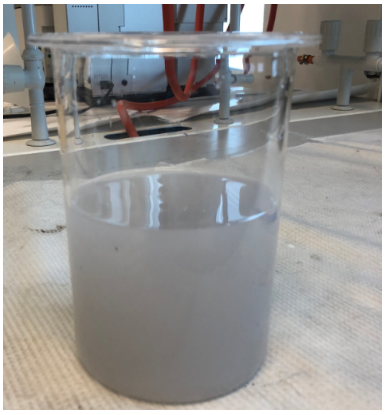

(c) Shows the color of the solution prior to irradiation

Figure 4.13: Shows the color of different solutions with dispersed B8.Rh powder, prior to and after irradiation

The tap water introduces variables that can not be controlled such as variation of ions in the water. A decision was made to continue with distilled water. The pH in water alters the reduction potential for H_2 in water and the oxidizing potential for

ethanol/methanol in water and therefore influencing the activity [74]. A previous study [56] showed that the photocatalytic activities were dependent on pH and the highest activity was obtained at pH 3,5. The study was performed for Rh doped $SrTiO_3$ loaded with Ru as co-catalyst.

4.5 Source of error

From the GC measurements report it could be seen that for some of the experiments performed, the detectors became unstable during the experiments. Sometimes they became more unstable for each measurement, and sometimes the detector appeared stable at the end of the experiments. All the experiments performed where the detectors have shown sign of instability has been disregarded completely in this report. The reason for the sudden instability in the detectors is believed to have been caused by vibrations in the building due to construction work outside the laboratory. Figure 4.14 illustrates the ability of the setup to reproduce results

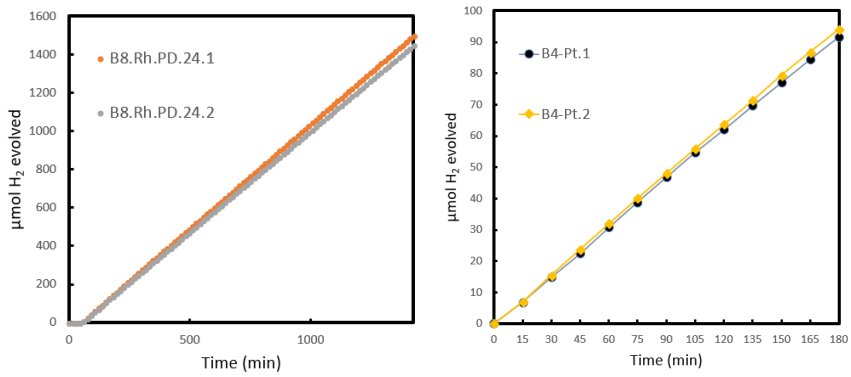

(a) Shows repeated experiment of B8.Rh.PD for 24 hours

(b) Shows repeated experiment of B4-Pt for 3 hours

Figure 4.14: shows reproduce ability of the setup

As can be seen from figure 4.14 the H_2 evolution is stable, and the same sample is producing an ~ equal amount of H_2 further indicating that the challenge to reproduce results and the sudden instability in the GC detectors, was induced by external conditions.

Chapter 5

Conclusion

All the samples were prepared with by solid state reaction method with the intended ratio of Sr/(Ti+Rh) = 1,02. The XRD specter shows the characteristic peaks for $SrTiO_3$. Some minor impurity peaks were also found in the XRD spectra for all samples. XRF revealed that there are more substances in the top layer of the sample after calcination in a high-temperature furnace, indicating that there is some contamination coming from the furnace. The ICP-MS Showed a variation in the Sr/(Ti+Rh) for the samples measured, indicating that the samples are not entirely homogeneous. The absorbance spectra of the samples were found by DRS measurements. The band gap found for $SrTiO_3$ are in accordance with literature, but the band gaps found for the Rh doped $SrTiO_3$ were wider than the band gaps reported. The absorbance spectra of Rh doped $SrTiO_3$, calcined at 1100 °C is well in accordance with literature, while the Rh doped samples calcined at 1000 °C were not as easy to compare. None of the synthesized photocatalyst samples evolved any detectable amount of H_2 without a co-catalyst, but the commercial TiO_2 P25 did. The pure $SrTiO_3$ performed better then the 1% Rh doped $SrTiO_3$ sample calcined at 1000°C, but the H_2 evolution was decreasing with time. The reason for the decreasing H_2 evolution has not been uncovered. With photodeposited Pt, The 1% Rh doped $SrTiO_3$ sample calcined at 1000°C did not perform significantly better then the pure $SrTiO_3$ and the APQ was lower. The 2% Rh doped $SrTiO_3$ sample was evolving H_2 at a lower rate than the pure $SrTiO_3$ with photodeposited Pt. The B8.Rh

yielded the highest H_2 evolution of all the synthesized samples, with photodeposited Pt. In addition, a color change, from dark grey/purple to yellow, in the solution could be observed for the B8.Rh, also in accordance with literature. It is believed that $SrTiO_3$ was successfully synthesized and that Rh doped $SrTiO_3$ was successfully synthesized at calcination temperature 1100 °C. Although the sample was successfully synthesized the commercial TiO2 P25 powder purchased from Sigma Aldrich evolved H_2 at a much higher rate than the B8.Rh. No detectable amounts of H_2 could be detected for the activity measurements with the CQD's.

Chapter 6

Further work

The optimal doping level of Rh in $SrTiO_3$ has already been investigated [9], [10] and the TiO_2 P25 showed a much higher activity than the synthesized samples by the solid state reaction method; the synthesis method should be further investigated. Preparation through different synthesis methods such as the hydrothermal method and the sol-gel method, both mentioned in the theory chapter, would also be helpful for confirming, and comparing the prepared material. There is also another preparation method called polymerizable complex method described in [10]. The technique is a modified sol-gel approach and is known as a powerful method for synthesizing highly homogeneous ceramics [10], [27]. Obtaining a homogeneous sample is important, not only for the doping, but also for the Sr/(Ti+Rh) ratio. As the last samples prepared and submitted for ICP-MS analysis, but not analyzed in time before the project finished, determining the amount of Pt loaded on to the photocatalyst after the photoreaction, remains. It would also be interesting with an ICP-MS analysis of an I-R prepared photocatalyst prior to and after the photoreaction to see if the amount of Pt is the same. Then there are the carbon quantum dots. Because the carbon quantum dots have been proven to enhance photocatalytic activity [37]–[39], solving the problem of why there was no photocatalytic activity in the presence of the CQDs is also an issue. Therefore, reviewing the synthesis and deposition method is necessary. It would also be good to submit the CQDs for photoluminescence analysis to see if the synthesized CQDs

possess the upconversion photoluminescence property described in [37]–[39]. A Z-scheme photocatalytic water splitting system, using $BiVO_4$ and $SrTiO_3$ loaded with Ru as O_2 and H_2 photocatalysts, respectively, was improved in [75] by using photoreduced graphene oxide as a solid electron mediator. It is believed that the CQD's facilitate electron transfer [38], it would be interesting to recreate the Z-scheme system and replace the photoreduced graphene oxide with CQD's.

Bibliography

[1] C. GRIMES, O. VARGHESE, and S. RANJAN, *Light, water, hydrogen: the solar generation of hydrogen by water photoelectrolysis*. Springer Science & Business Media, 2007.

[2] J. Hansen, M. Sato, P. Kharecha, D. Beerling, R. Berner, V. Masson-Delmotte, M. Pagani, M. Raymo, D. L. Royer, and J. C. Zachos, "Target atmospheric co2: Where should humanity aim?" *arXiv preprint arXiv:0804.1126*, 2008.

[3] J. Rockström, W. Steffen, K. Noone, Å. Persson, F. S. Chapin III, E. F. Lambin, T. M. Lenton, M. Scheffer, C. Folke, H. J. Schellnhuber, *et al.*, "A safe operating space for humanity," *nature*, vol. 461, no. 7263, p. 472, 2009.

[4] P. Moriarty and D. Honnery, "What is the global potential for renewable energy?" *Renewable and Sustainable Energy Reviews*, vol. 16, no. 1, pp. 244–252, 2012.

[5] V. Jovic, Z. H. Al-Azri, W.-T. Chen, D. Sun-Waterhouse, H Idriss, and G. I. Waterhouse, "Photocatalytic h2 production from ethanol–water mixtures over pt/tio2 and au/tio2 photocatalysts: A comparative study," *Topics in Catalysis*, vol. 56, no. 12, pp. 1139–1151, 2013.

[6] A. Kudo and Y. Miseki, "Heterogeneous photocatalyst materials for water splitting," *Chemical Society Reviews*, vol. 38, no. 1, pp. 253–278, 2009.

[7] M. R. Gholipour, C.-T. Dinh, F. Béland, and T.-O. Do, "Nanocomposite heterojunctions as sunlight-driven photocatalysts for hydrogen production from water splitting," *Nanoscale*, vol. 7, no. 18, pp. 8187–8208, 2015.

[8] R. Konta, T. Ishii, H. Kato, and A. Kudo, "Photocatalytic activities of noble metal ion doped srtio3 under visible light irradiation," *The Journal of Physical Chemistry B*, vol. 108, no. 26, pp. 8992–8995, 2004.

[9] Y. Kuo and K. J. Klabunde, "Hydrogen generation from water/methanol under visible light using aerogel prepared strontium titanate (srtio3) nanomaterials doped with ruthenium and rhodium metals," *Nanotechnology*, vol. 23, no. 29, p. 294 001, 2012.

[10] H. Kato, Y. Sasaki, N. Shirakura, and A. Kudo, "Synthesis of highly active rhodium-doped srtio 3 powders in z-scheme systems for visible-light-driven photocatalytic overall water splitting," *Journal of Materials Chemistry A*, vol. 1, no. 39, pp. 12 327–12 333, 2013.

[11] H. S. Fogler, "Elements of chemical reaction engineering," 2016.

[12] S. Sze and M.-K. Lee, "Semiconductor devices: Physics and technology," 2012.

[13] H. Kisch, *Semiconductor photocatalysis: principles and applications*. John Wiley & Sons, 2014.

[14] J. Phillips, *Bonds and Bands in Semiconductors : Second Edition*. Momentum Press, 2010, vol. 2nd ed, ISBN: 9781606501337. [Online]. Available: `http://search.ebscohost.com/login.aspx?direct=true&db=nlebk&AN=501169&site=ehost-live`.

[15] B. Wardle, *Principles and applications of photochemistry*. John Wiley & Sons, 2009.

[16] M. A. Fox and M. T. Dulay, "Heterogeneous photocatalysis," *Chemical reviews*, vol. 93, no. 1, pp. 341–357, 1993.

[17] J.-M. Herrmann, "Heterogeneous photocatalysis: State of the art and present applications in honor of pr. rl burwell jr.(1912–2003), former head of ipatieff laboratories, northwestern university, evanston (ill).," *Topics in Catalysis*, vol. 34, no. 1, pp. 49–65, 2005.

[18] B. S. Hugo de Lasa and M. Salaices, *Photocatalytic Reaction engineering*. Springer, 2005.

[19] I. Chorkendorff and J. Niemantsverdiet, *Concepts of Modern Catalysis and Kinetics*. Wiley-VCH, 2003.

[20] E. Glover, S. Ellington, G Sankar, and R. Palgrave, "The nature and effects of rhodium and antimony dopants on the electronic structure of tio 2: Towards design of z-scheme photocatalysts," *Journal of Materials Chemistry A*, vol. 4, no. 18, pp. 6946–6954, 2016.

[21] R. Wang, K.-Q. Lu, Z.-R. Tang, and Y.-J. Xu, "Recent progress in carbon quantum dots: Synthesis, properties and applications in photocatalysis," *Journal of Materials Chemistry A*, vol. 5, no. 8, pp. 3717–3734, 2017.

[22] E. H. Sargent, "Infrared photovoltaics made by solution processing," *Nature Photonics*, vol. 3, no. 6, pp. 325–331, 2009.

[23] S. C. Apan, "Photocatalysis masters," Master's thesis, Norwegian University of Science and Technology, 2016.

[24] K. Iwashina and A. Kudo, "Rh-doped srtio3 photocatalyst electrode showing cathodic photocurrent for water splitting under visible-light irradiation," *Journal of the American Chemical Society*, vol. 133, no. 34, pp. 13 272–13 275, 2011.

[25] B. B. Lakshmi, P. K. Dorhout, and C. R. Martin, "Sol- gel template synthesis of semiconductor nanostructures," *Chemistry of materials*, vol. 9, no. 3, pp. 857–862, 1997.

[26] M. Anpo and M. Takeuchi, "The design and development of highly reactive titanium oxide photocatalysts operating under visible light irradiation," *Journal of catalysis*, vol. 216, no. 1-2, pp. 505–516, 2003.

[27] P. Shen, J. C. Lofaro Jr, W. R. Woerner, M. G. White, D. Su, and A. Orlov, "Photocatalytic activity of hydrogen evolution over rh doped srtio3 prepared by polymerizable complex method," *Chemical engineering journal*, vol. 223, pp. 200–208, 2013.

[28] E. Marceau, X. Carrier, and M. Che, "Impregnation and drying," *Synthesis of Solid Catalysts*, pp. 59–83, 2009.

[29] J. T. Richardson, *Principles of catalyst development*. Plenum Press, New York, 1989.

[30] J. Haber, J. Block, and B Delmon, "Manual of methods and procedures for catalyst characterization (technical report)," *Pure and applied Chemistry*, vol. 67, no. 8-9, pp. 1257–1306, 1995.

[31] J. Hagen, *Industrial catalysis: a practical approach*. John Wiley & Sons, 2015.

[32] X. Jiang, X. Fu, L. Zhang, S. Meng, and S. Chen, "Photocatalytic reforming of glycerol for h 2 evolution on pt/tio 2: Fundamental understanding the effect of co-catalyst pt and the pt deposition route," *Journal of Materials Chemistry A*, vol. 3, no. 5, pp. 2271–2282, 2015.

[33] Y. Sasaki, A. Iwase, H. Kato, and A. Kudo, "The effect of co-catalyst for z-scheme photocatalysis systems with an fe3+/fe2+ electron mediator on overall water splitting under visible light irradiation," *Journal of Catalysis*, vol. 259, no. 1, pp. 133–137, 2008.

[34] H. M. McNair and J. M. Miller, *Basic gas chromatography*. John Wiley & Sons, 2011.

[35] D. C. Harris, *Quantitative chemical analysis*. WH Freeman New York, 2010, vol. EIGHTH EDITION.

[36] X. Xu, R. Ray, Y. Gu, H. J. Ploehn, L. Gearheart, K. Raker, and W. A. Scrivens, "Electrophoretic analysis and purification of fluorescent single-walled carbon nanotube fragments," *Journal of the American Chemical Society*, vol. 126, no. 40, pp. 12 736–12 737, 2004.

[37] H. Li, X. He, Z. Kang, H. Huang, Y. Liu, J. Liu, S. Lian, C. H. A. Tsang, X. Yang, and S.-T. Lee, "Water-soluble fluorescent carbon quantum dots and photocatalyst design," *Angewandte Chemie International Edition*, vol. 49, no. 26, pp. 4430–4434, 2010.

[38] S. Y. Lim, W. Shen, and Z. Gao, "Carbon quantum dots and their applications," *Chemical Society Reviews*, vol. 44, no. 1, pp. 362–381, 2015.

[39] M. Zhu, X. Deng, X. Lin, L. Zhang, W. Zhang, Y. Lv, and J. Pan, "The carbon quantum dots modified zno/tio 2 nanotube heterojunction and its visible light photocatalysis enhancement," *Journal of Materials Science: Materials in Electronics*, pp. 1–8,

[40] R. R. Islangulov, D. V. Kozlov, and F. N. Castellano, "Low power upconversion using mlct sensitizers," *Chemical Communications*, no. 30, pp. 3776–3778, 2005.

[41] H. Scientific. (). X-ray fluorescence - the basic process, [Online]. Available: `http://www.horiba.com/scientific/products/x-ray-fluorescence-`

analysis/tutorial/x-ray-fluorescence-the-basic-process/ (visited on 11/09/2017).

[42] E. Margui and R. van Grieken, *X-Ray Fluorescence Spectrometry and Related Techniques: An Introduction*. Momentum Press, New York, 2013.

[43] G Leofanti, G Tozzola, M Padovan, G Petrini, S Bordiga, and A Zecchina, "Catalyst characterization: Characterization techniques," *Catalysis today*, vol. 34, no. 3-4, pp. 307–327, 1997.

[44] B Ohtani, "Photocatalysis a to z—what we know and what we do not know in a scientific sense," *Journal of Photochemistry and Photobiology C: Photochemistry Reviews*, vol. 11, no. 4, pp. 157–178, 2010.

[45] L. Wang, G. Liang, and G. Dang, "A study on the protection to relics and the related problems with diffuse reflectance spectroscopy," *Spectrochimica Acta Part A: Molecular and Biomolecular Spectroscopy*, vol. 61, no. 5, pp. 1021–1024, 2005.

[46] A. M. Beale, E. Stavitski, and B. M. Weckhuysen, "Characterization of catalysts: Surface and in-situ methods," *Encyclopedia of life support systems (EOLSS). Available at*, 2015.

[47] D. G. Barton, M. Shtein, R. D. Wilson, S. L. Soled, and E. Iglesia, "Structure and electronic properties of solid acids based on tungsten oxide nanostructures," *The Journal of Physical Chemistry B*, vol. 103, no. 4, pp. 630–640, 1999.

[48] U. X. t. Cambridge. (2017), [Online]. Available: https://www.doitpoms.ac.uk/tlplib/xray-diffraction/index.php (visited on 10/12/2017).

[49] P. Ruth E. Wolf. (). What is icp-ms? [Online]. Available: https://crustal.usgs.gov/laboratories/icpms/intro.html (visited on 04/04/2018).

[50] Udani, P.P.C. and Rønning, M., "Comparative study on the photocatalytic hydrogen production from methanol over cu-, pd-, co- and au-loaded tio2," *Oil Gas Sci. Technol. – Rev. IFP Energies nouvelles*, vol. 70, no. 5, pp. 831–839, 2015. DOI: 10.2516/ogst/2015025. [Online]. Available: https://doi.org/10.2516/ogst/2015025.

[51] K Karthick, S. R. Ede, U Nithiyanantham, and S. Kundu, "Low-temperature synthesis of srtio 3 nanoassemblies on dna scaffolds and their applications

in dye-sensitized solar cells and supercapacitors," *New Journal of Chemistry*, vol. 41, no. 9, pp. 3473–3486, 2017.

[52] Z. Wu, X. Wang, Z. Zou, *et al.*, "Ag@ srtio3 nanocomposite for super photocatalytic degradation of organic dye and catalytic reduction of 4-nitrophenol," *New Journal of Chemistry*, 2017.

[53] P. Jing, J. Du, J. Wang, W. Lan, L. Pan, J. Li, J. Wei, D. Cao, X. Zhang, C. Zhao, *et al.*, "Hierarchical srtio 3/nife 2 o 4 composite nanostructures with excellent light response and magnetic performance synthesized toward enhanced photocatalytic activity," *Nanoscale*, vol. 7, no. 35, pp. 14 738–14 746, 2015.

[54] M. N. Ha, F. Zhu, Z. Liu, L. Wang, L. Liu, G. Lu, and Z. Zhao, "Morphology-controlled synthesis of srtio 3/tio 2 heterostructures and their photocatalytic performance for water splitting," *RSC Advances*, vol. 6, no. 25, pp. 21 111–21 118, 2016.

[55] S. Okunaka, H. Tokudome, and R. Abe, "Facile water-based preparation of rh-doped srtio 3 nanoparticles for efficient photocatalytic h 2 evolution under visible light irradiation," *Journal of Materials Chemistry A*, vol. 3, no. 28, pp. 14 794–14 800, 2015.

[56] Y. Sasaki, H. Nemoto, K. Saito, and A. Kudo, "Solar water splitting using powdered photocatalysts driven by z-schematic interparticle electron transfer without an electron mediator," *The Journal of Physical Chemistry C*, vol. 113, no. 40, pp. 17 536–17 542, 2009.

[57] A. R. West, *Solid state chemistry and its applications*. John Wiley & Sons, 2014.

[58] X. Pan, X. Chen, and Z. Yi, "Photocatalytic oxidation of methane over srco 3 decorated srtio 3 nanocatalysts via a synergistic effect," *Physical Chemistry Chemical Physics*, vol. 18, no. 46, pp. 31 400–31 409, 2016.

[59] J. Wang, S. Yin, Q. Zhang, F. Saito, and T. Sato, "Mechanochemical synthesis of srtio 3- x f x with high visible light photocatalytic activities for nitrogen monoxide destruction," *Journal of Materials Chemistry*, vol. 13, no. 9, pp. 2348–2352, 2003.

[60] A. Kudo, A. Tanaka, K. Domen, and T. Onishi, “The effects of the calcination temperature of srtio3 powder on photocatalytic activities,” *Journal of Catalysis*, vol. 111, no. 2, pp. 296–301, 1988.

[61] S. Hara, M. Yoshimizu, S. Tanigawa, L. Ni, B. Ohtani, and H. Irie, “Hydrogen and oxygen evolution photocatalysts synthesized from strontium titanate by controlled doping and their performance in two-step overall water splitting under visible light,” *The Journal of Physical Chemistry C*, vol. 116, no. 33, pp. 17 458–17 463, 2012.

[62] H. Yu, J. Wang, S. Yan, T. Yu, and Z. Zou, “Elements doping to expand the light response of srtio3,” *Journal of Photochemistry and Photobiology A: Chemistry*, vol. 275, pp. 65–71, 2014.

[63] H. Yu, S. Ouyang, S. Yan, Z. Li, T. Yu, and Z. Zou, “Sol–gel hydrothermal synthesis of visible-light-driven cr-doped srtio 3 for efficient hydrogen production,” *Journal of Materials Chemistry*, vol. 21, no. 30, pp. 11 347–11 351, 2011.

[64] R. I. Bickley, T. Gonzalez-Carreno, J. S. Lees, L. Palmisano, and R. J. Tilley, “A structural investigation of titanium dioxide photocatalysts,” *Journal of Solid State Chemistry*, vol. 92, no. 1, pp. 178–190, 1991.

[65] R. López and R. Gómez, “Band-gap energy estimation from diffuse reflectance measurements on sol–gel and commercial tio2: A comparative study,” *Journal of sol-gel science and technology*, vol. 61, no. 1, pp. 1–7, 2012.

[66] P. K. Gogoi and D. Schmidt, “Temperature-dependent dielectric function of bulk srtio 3: Urbach tail, band edges, and excitonic effects,” *Physical Review B*, vol. 93, no. 7, p. 075 204, 2016.

[67] S. Zhang, D. Guo, M. Wang, M. S. Javed, and C. Hu, “Magnetism in srtio3 before and after uv irradiation,” *Applied Surface Science*, vol. 335, pp. 115–120, 2015.

[68] M Avudaithai and T. Kutty, “Ultrafine powders of srtio3 from the hydrothermal preparation and their catalytic activity in the photolysis of water,” *Materials research bulletin*, vol. 22, no. 5, pp. 641–650, 1987.

[69] M. Zubair, A. Razzaq, C. A. Grimes, and S.-I. In, “Cu2znsns4 (czts)-zno: A noble metal-free hybrid z-scheme photocatalyst for enhanced solar-spectrum

photocatalytic conversion of co2 to ch4," *Journal of CO2 Utilization*, vol. 20, pp. 301–311, 2017.

[70] W.-N. Wang, W.-J. An, B. Ramalingam, S. Mukherjee, D. M. Niedzwiedzki, S. Gangopadhyay, and P. Biswas, "Size and structure matter: Enhanced co2 photoreduction efficiency by size-resolved ultrafine pt nanoparticles on tio2 single crystals," *Journal of the American chemical society*, vol. 134, no. 27, pp. 11 276–11 281, 2012.

[71] W.-J. Ong, L.-L. Tan, S.-P. Chai, S.-T. Yong, and A. R. Mohamed, "Self-assembly of nitrogen-doped tio 2 with exposed 001 facets on a graphene scaffold as photo-active hybrid nanostructures for reduction of carbon dioxide to methane," *Nano Research*, vol. 7, no. 10, pp. 1528–1547, 2014.

[72] L. Liu, Y. Jiang, H. Zhao, J. Chen, J. Cheng, K. Yang, and Y. Li, "Engineering coexposed 001 and 101 facets in oxygen-deficient tio2 nanocrystals for enhanced co2 photoreduction under visible light," *ACS Catalysis*, vol. 6, no. 2, pp. 1097–1108, 2016.

[73] A. Patsoura, D. I. Kondarides, and X. E. Verykios, "Photocatalytic degradation of organic pollutants with simultaneous production of hydrogen," *Catalysis Today*, vol. 124, no. 3-4, pp. 94–102, 2007.

[74] J. Chen, D. F. Ollis, W. H. Rulkens, and H. Bruning, "Photocatalyzed oxidation of alcohols and organochlorides in the presence of native tio2 and metallized tio2 suspensions. part (i): Photocatalytic activity and ph influence," *Water Research*, vol. 33, no. 3, pp. 661–668, 1999.

[75] A. Iwase, Y. H. Ng, Y. Ishiguro, A. Kudo, and R. Amal, "Reduced graphene oxide as a solid-state electron mediator in z-scheme photocatalytic water splitting under visible light," *Journal of the American Chemical Society*, vol. 133, no. 29, pp. 11 054–11 057, 2011.

Appendix A

N_2 Physisorption

This appendix contains one summary report along with the linear isotherm plot from the N_2 physisorption measurements. This part is only provided to serve as an example for finding the BET surface area. The only data used from the N_2 measurements are the BET surface area.

Full Report Set

Sample: SrTiO3 batch 3.0
Operator: Dani
File: C:\Users\labuser\Desktop\BET data from ...\000-043.SMP

Started:	16.11.2017 22:43:51	Analysis Adsorptive:	N2
Completed:	17.11.2017 10:18:22	Analysis Bath Temp.:	-195,850 °C
Report Time:	25.06.2018 02:03:30	Thermal Correction:	No
Sample Mass:	0,0559 g	Warm Free Space:	12,5184 cm³ Measured
Cold Free Space:	37,6190 cm³	Equilibration Interval:	10 s
Low Pressure Dose:	None	Sample Density:	1,000 g/cm³
Automatic Degas:	No		

Summary Report

Surface Area

Single point surface area at p/p° = 0,300144933: 6,8485 m²/g

BET Surface Area: 7,1077 m²/g

BJH Adsorption cumulative surface area of pores between 17,000 Å and 3 000,000 Å width: 4.591 m²/g

BJH Desorption cumulative surface area of pores between 17,000 Å and 3 000,000 Å width: 5,8546 m²/g

Pore Volume

Single point desorption total pore volume of pores less than 915,466 Å width at p/p° = 0,978385253: 0,010811 cm³/g

BJH Adsorption cumulative volume of pores between 17,000 Å and 3 000,000 Å width: 0,008803 cm³/g

BJH Desorption cumulative volume of pores between 17,000 Å and 3 000,000 Å width: 0,009699 cm³/g

Pore Size

Desorption average pore diameter (4V/A by BET): 60,8433 Å

BJH Adsorption average pore width (4V/A): 76,698 Å

BJH Desorption average pore width (4V/A): 66,264 Å

DFT Pore Size

Volume in Pores	<	9,51 Å	:	0,00066 cm³/g
Total Volume in Pores	<=	448,83 Å	:	0,00966 cm³/g
Total Area in Pores	>=	9,51 Å	:	7,478 m²/g

Nanoparticle Size:

Average Particle Size 8 441,588 Å

Sample: SrTiO3 batch 3.0
Operator: Dani
File: C:\Users\labuser\Desktop\BET data from ...\000-043.SMP

Started:	16.11.2017 22:43:51	Analysis Adsorptive:	N2
Completed:	17.11.2017 10:18:22	Analysis Bath Temp.:	-195,850 °C
Report Time:	25.06.2018 02:03:30	Thermal Correction:	No
Sample Mass:	0,0559 g	Warm Free Space:	12,5184 cm³ Measured
Cold Free Space:	37,6190 cm³	Equilibration Interval:	10 s
Low Pressure Dose:	None	Sample Density:	1,000 g/cm³
Automatic Degas:	No		

Isotherm Linear Plot

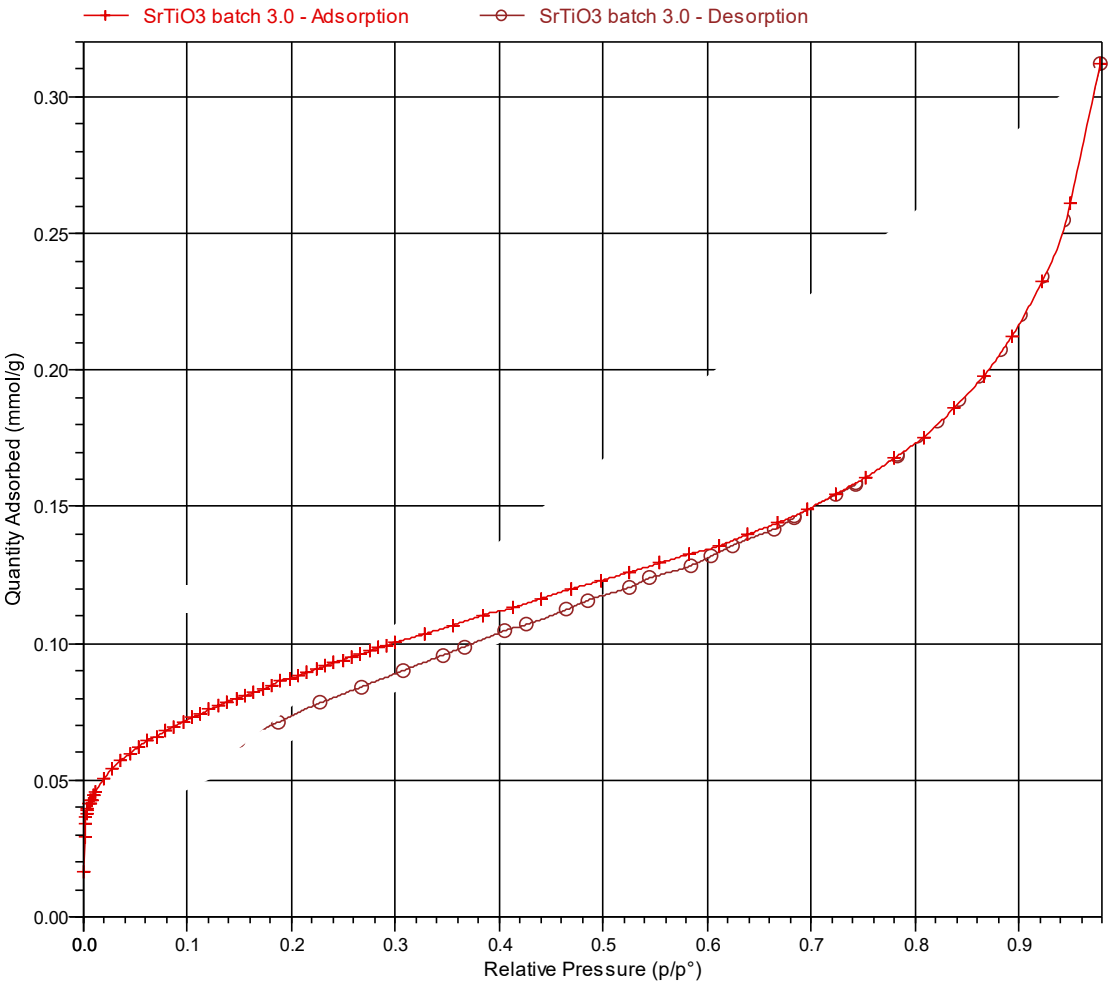

Appendix B

XRD

This appendix contains all of the XRD spectras, used in figure 4.1, 4.2, 4.4 and 4.5. In addition, There is included a possible match for the impurity peaks, provided by the XRD analysis software.

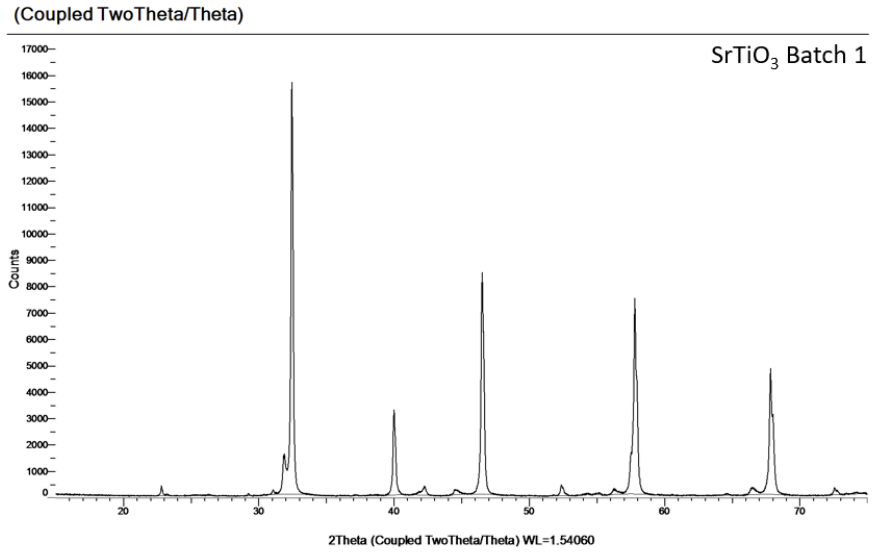

Figure B.1: Shows the XRD spectra of $SrTiO_3$ from Batch 1

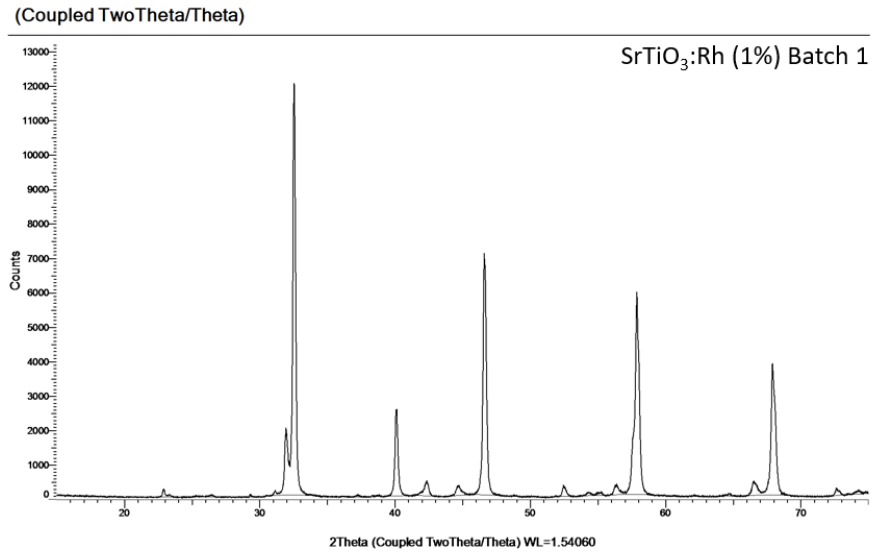

Figure B.2: Shows the XRD spectra of $SrTiO_3$:Rh (1%) from Batch 1

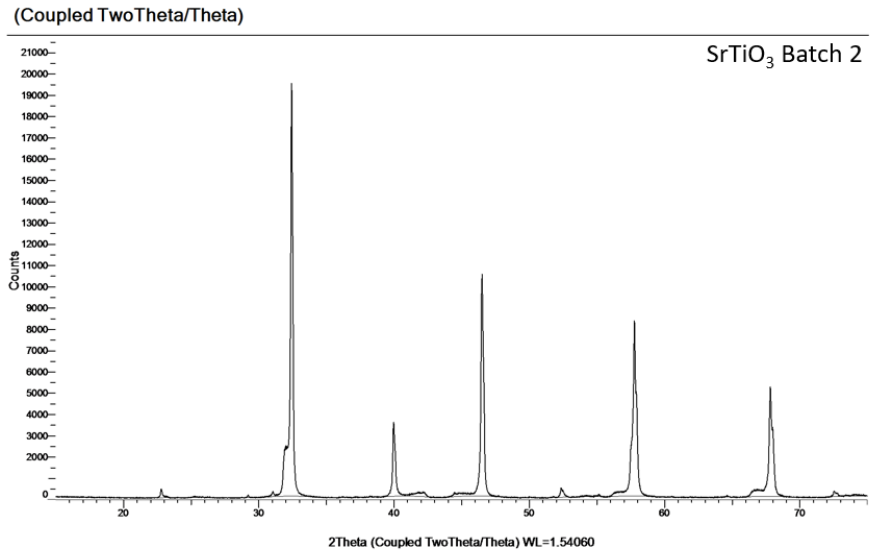

Figure B.3: Shows the XRD spectra of $SrTiO_3$ from Batch 2

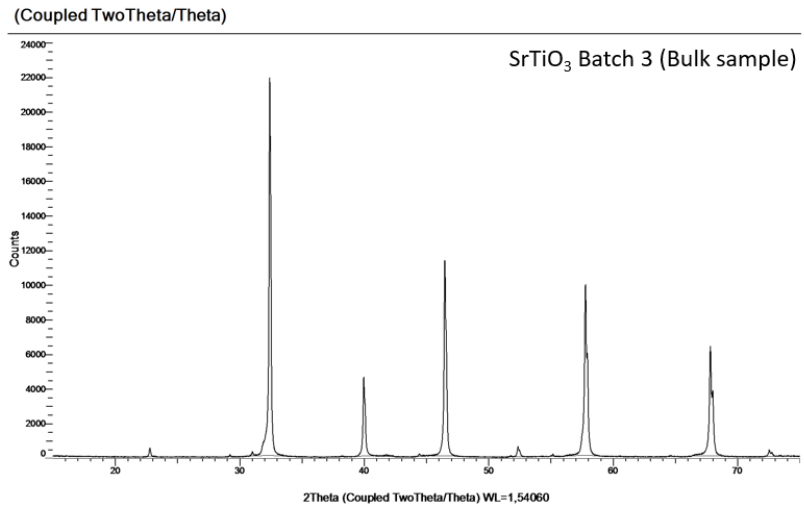

Figure B.4: Shows the XRD spectra of $SrTiO_3$ from Batch 3, bulk sample

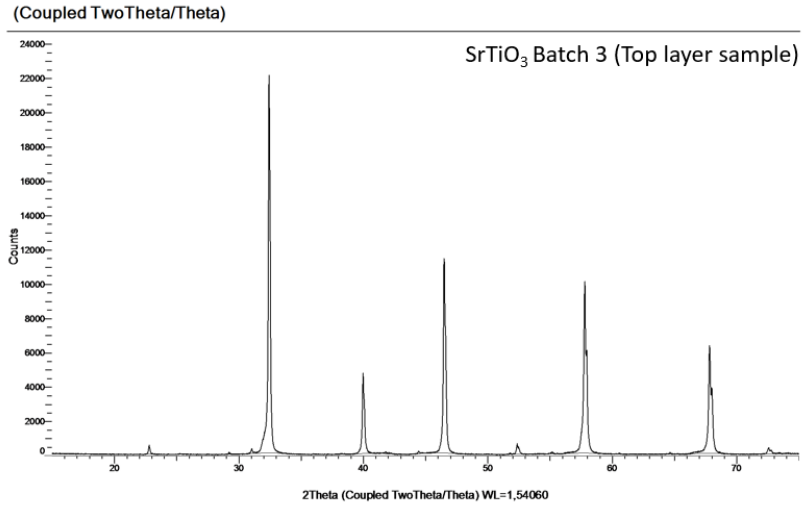

Figure B.5: Shows the XRD spectra of $SrTiO_3$ from Batch 3 sample of the top layer

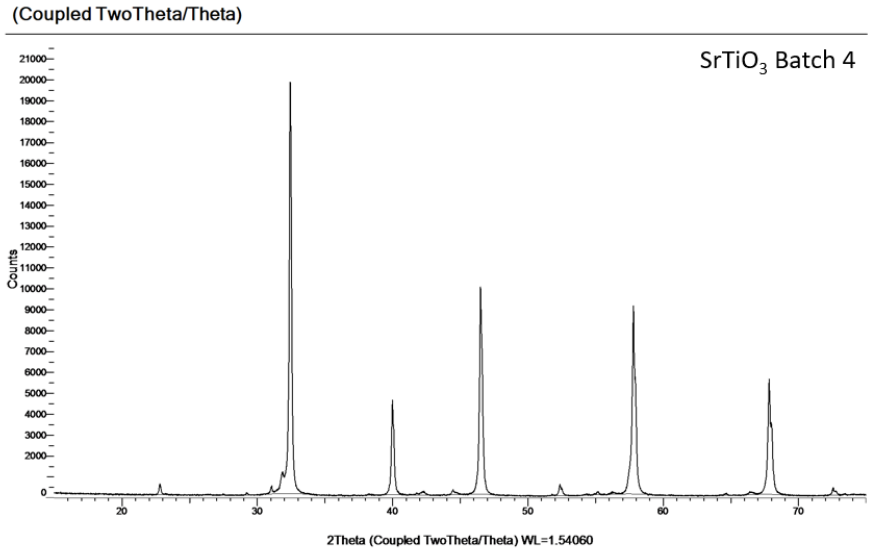

Figure B.6: Shows the XRD spectra of $SrTiO_3$ from Batch 4

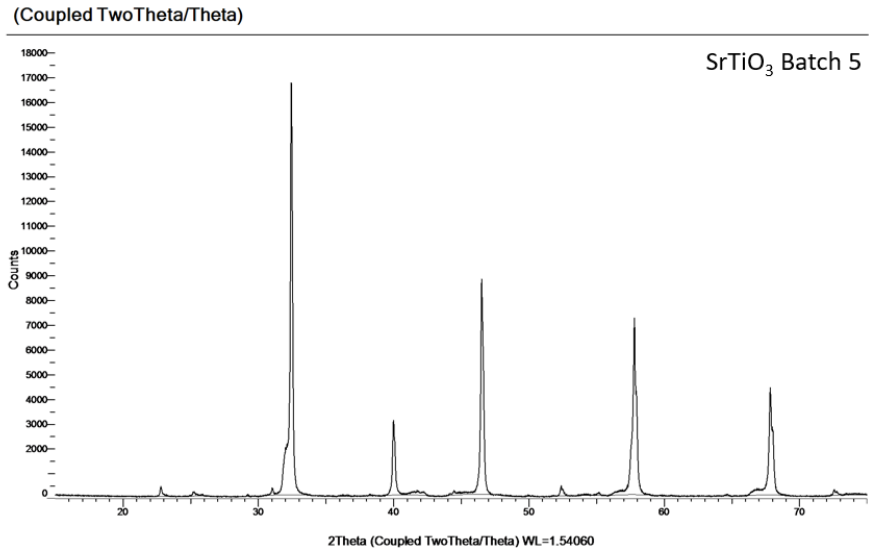

Figure B.7: Shows the XRD spectra of $SrTiO_3$ from Batch 5

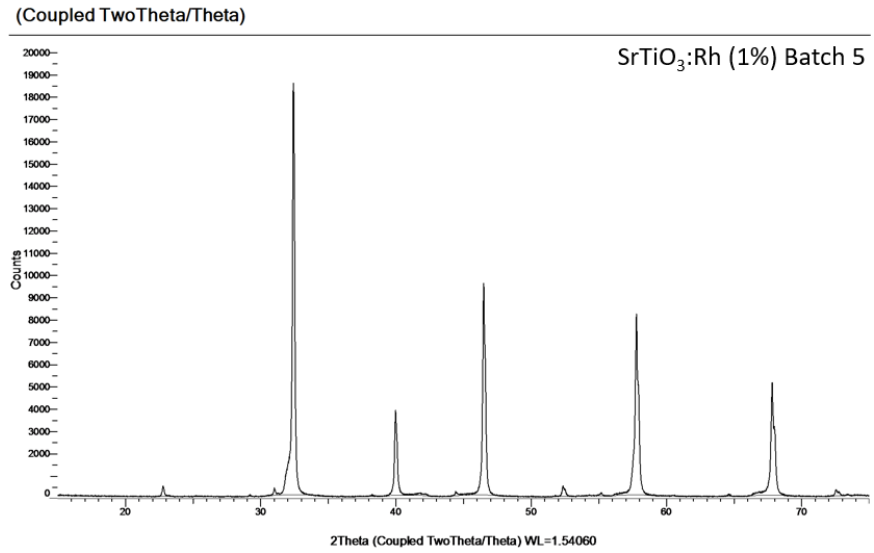

Figure B.8: Shows the XRD spectra of $SrTiO_3$ from Batch 5

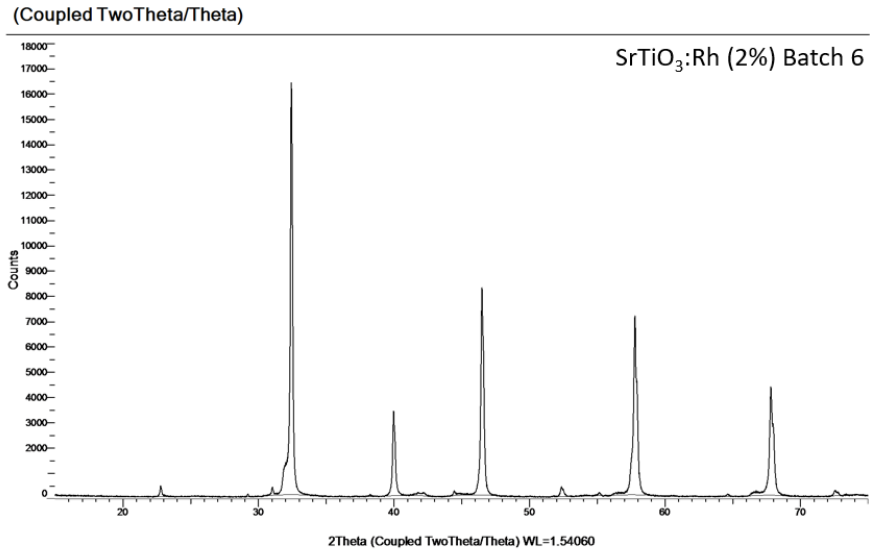

Figure B.9: Shows the XRD spectra of $SrTiO_3$:Rh (2%) from Batch 6

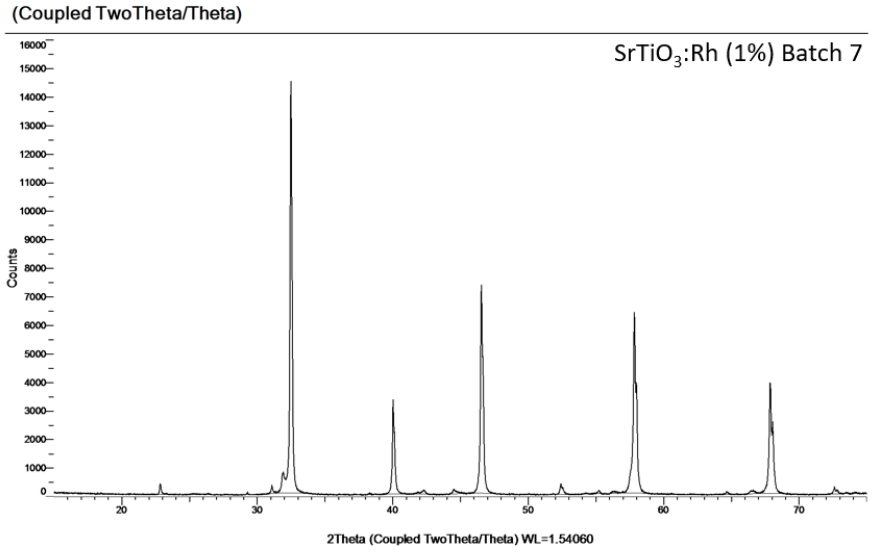

Figure B.10: Shows the XRD spectra of $SrTiO_3$:Rh (1%) from Batch 7

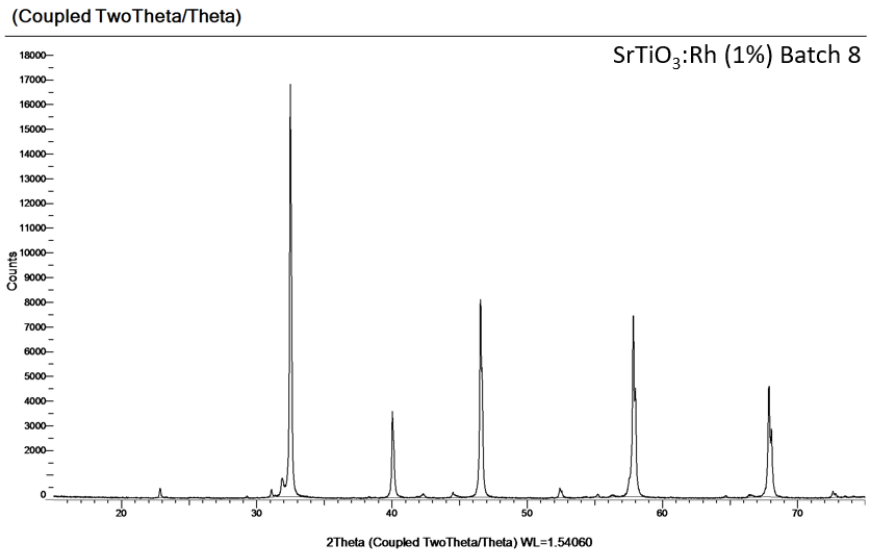

Figure B.11: Shows the XRD spectra of $SrTiO_3$:Rh (1%) from Batch 8

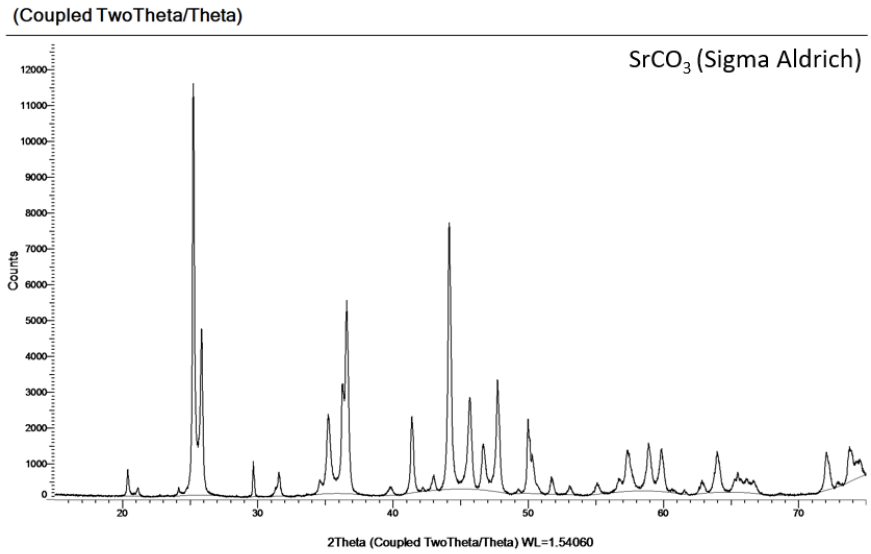

Figure B.12: Shows the XRD spectra of $SrCO_3$ from Sigma Aldrich

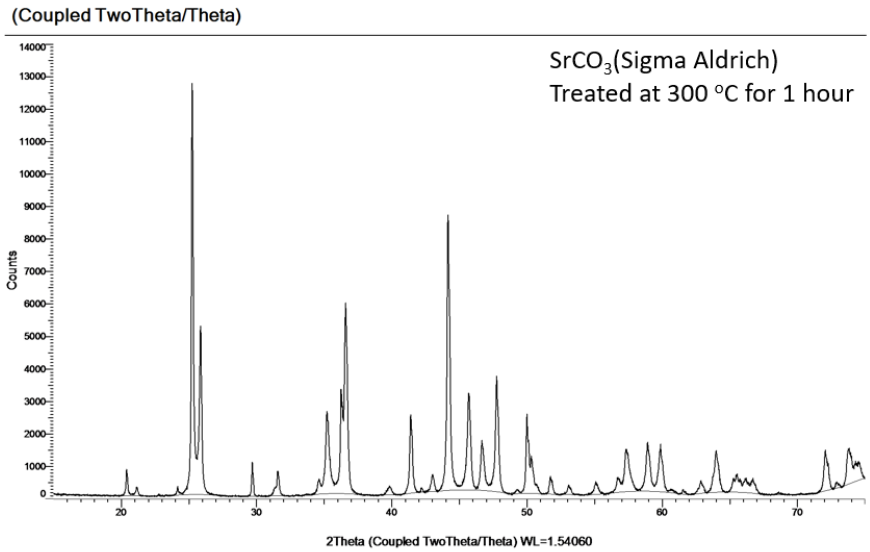

Figure B.13: Shows the XRD spectra of $SrCO_3$ treated at 300 ^{circ}C for 1 hour, from Sigma Aldrich

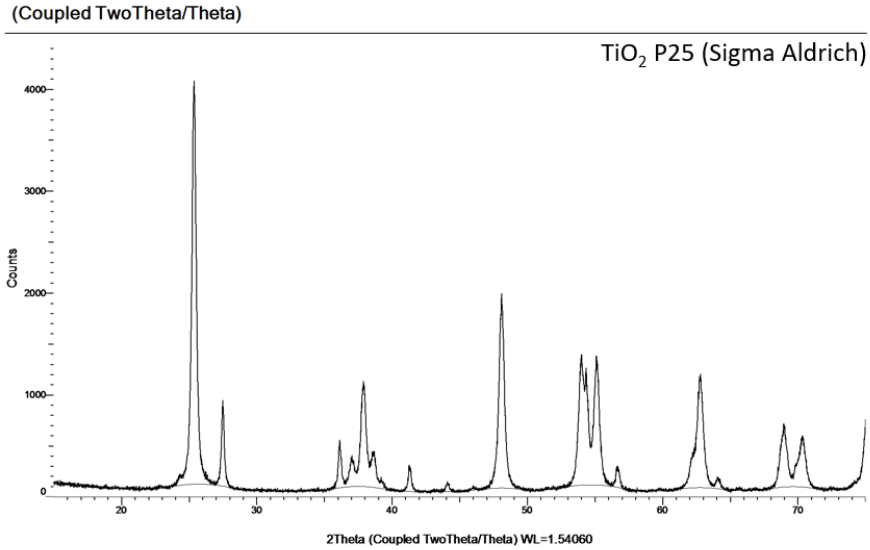

Figure B.14: Shows the XRD spectra of TiO_2 (P25) from Sigma Aldrich

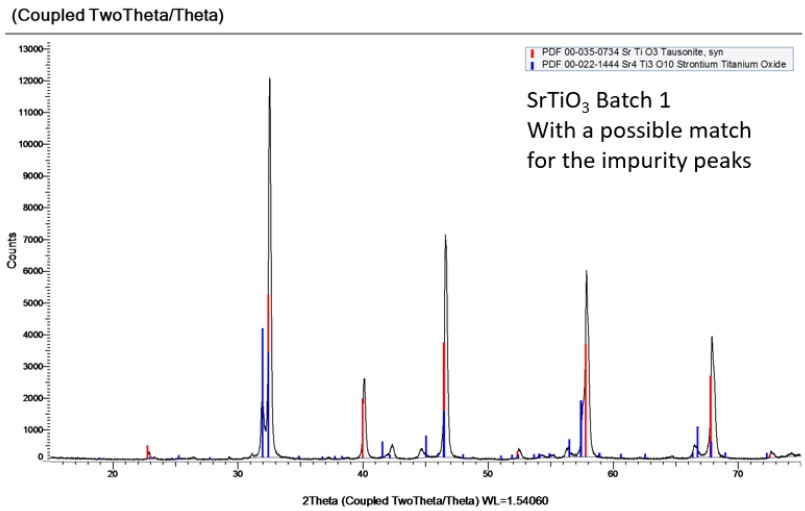

Figure B.15: Shows the XRD spectra of $SrTiO_3$ from Batch 1 with a possible match for the impurity peaks. Red coler is characteristics for $SrTiO_3$ and blue color is characteristic peaks for $Sr_4Ti_3O_7$

Appendix C

UV-vis DRS

Figure C.1 shows the full DRS spectra measured for B8.Rh

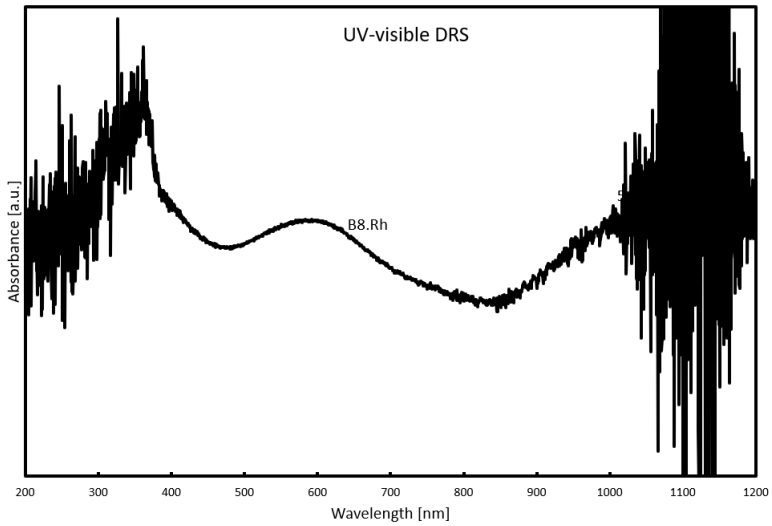

Figure C.1: Shows the full DRS specter of the B8.Rh

Appendix D

Some calculations

D.1 ICP-MS

The following calculation is presented as an example of how the stoichiometry was found.

Table D.1: A list of the precursor elements with the corresponding $\frac{g}{mol}$

Element	[g/mol]
Sr	87,62
Ti	47,867
Rh	102,906
O	15,999
C	12,011

Example for stochiometric $SrTiO_3$

87,67 [g] of Sr and 47,867 [g] of Ti is needed

For $SrTiO_3$:Rh with the stochiometric relatioship, $Sr_{1,02}$:$Ti_{0,99}$:$Rh_{0,01}$

the mole ratio $\frac{Sr[mole]}{(Ti+Rh)[mole]}$ = 1,02

If 1 mole of $SrTiO_3$:Rh (1%) is to be made

The amount of Sr is found by 1,02 [mole] × 87,62 [$\frac{g}{mole}$] = 89,372 [g]

The amount of Ti is found by 0,99 [mole] × 47,867 $[\frac{g}{mole}]$ =47,388 [g]

The amount of Rh is found by 0,01 [mole] × 102,906 $[\frac{g}{mole}]$ = 1,029 [g]

The amount of O is found by 3[mole] × 15,999 $[\frac{g}{mole}]$ = 47,997 [g]

The molar weight of $SrTiO_3$:Rh (1%) = 89,372 (Sr) + 47,388 (Ti) + 47,997 (O) 1,029 (Rh) = 185,786 $[\frac{g}{mole}]$

Optimal mass % is then found by dividing the element on the molar weight

For Sr: $\frac{89,372[g]}{185,786[g]}$ × 100 % = 48,1%

For Ti $\frac{47,388[g]}{185,786[g]}$ × 100 % = 25,5%

For Rh $\frac{1,029[g]}{185,786[g]}$ × 100 % = 0,554 %

D.2 Apparent quantum yield

Showing the equations used for finding the APQ.

$$\text{Number of reacted electrons} = 2 \times [H_2] \times N_A \tag{D.1}$$

$$\text{Total number of photons absorbed} = \frac{\text{Light absorbed by the photocatalyst}}{\text{The energy of the photon}} \times t \tag{D.2}$$

$$\text{Light absorbed by the photocatalyst} = H \times A \tag{D.3}$$

$$\text{The energy of the photon} = \frac{hc}{\lambda_{QY}} \tag{D.4}$$

$[H_2$ = moles of H_2 produced in time (t)

t = is the photoreaction time

H = 1000 $[\frac{W}{m^2}]$

A_{QY} = 0,0044156 $[m^2]$

c = 2,998 $\times 10^8 [\frac{m}{s}]$

h = 6,626 $\times$ 10^{-34} [J $\times$ s]

N_A = 6,022 $\times 10^{23} [\frac{1}{mole}]$

e = 1,602 $\times$ 10^{-19} $[\frac{C}{mol}]$

λ_{QY} = Average wavelength of broadband light source. Dependent on the band gap. For $SrTiO_3$ with band gap = 3,2 [eV] $\rightarrow$ $\lambda = \frac{387+250}{2}$ = 319 [nm]

Appendix E

Experimental details

E.1 P25 with and without PD Pt

Figure E.1 presents a comparison of the purchased TiO_2 P25 from Sigma Aldrich with and without photodeposited Pt. with experimental results listed in table E.1

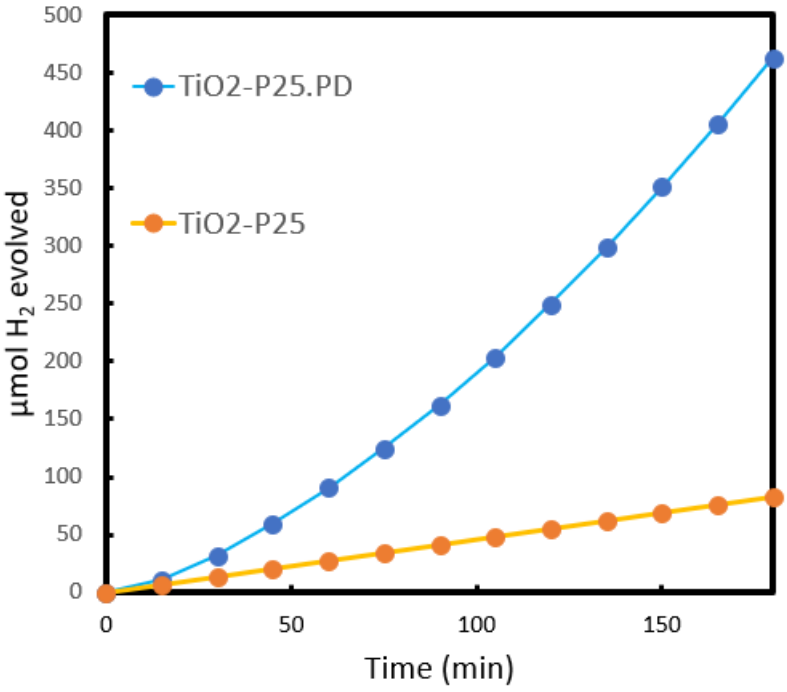

Figure E.1: Shows the activity measurement of TiO_2 P25 from sigma Aldrich, with and without PD Pt

Table E.1: Shows the experimental results for the TiO_2P25 with and without photodeposited Pt.

Experiment	Experiment duration [h]	induction time	$[\frac{\mu mole H_2}{hour}]$	APQ (%)
TiO_2-P25	3	0	27,6	0,13
TiO_2-P25.PD	24	0	274,2	1,24

E.2 Preliminary measurement of ethanol and methanol

Some of the preliminary results from the comparison between methanol and ethanol is shown in figure E.2.

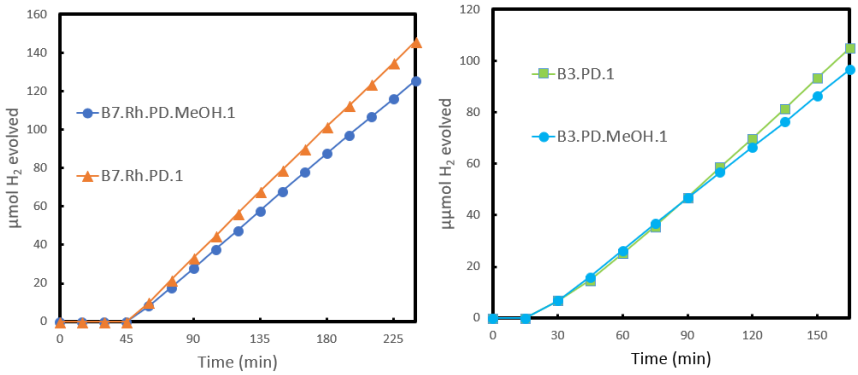

(a) shows a comparison between methanol and ethanol for PD Pt on B7.Rh

(b) shows a comparison between methanol and ethanol for PD Pt on B3

Figure E.2: shows some of the preliminary results of the comparison between methanol and ethanol

E.3 Experimental details

Figure E.3 shows a picture taken of the irradiated solution. From the picture it can be seen that the solution is absorbing all the light from the solar simulator.

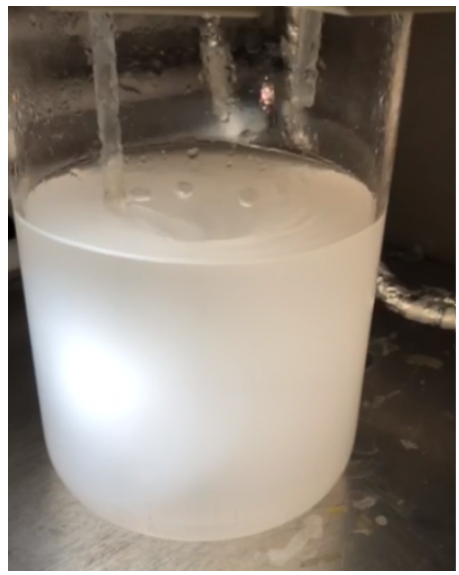

Figure E.3: Shows a picture of the irradiated solution absorbing all of the light from the solar simulator

E.4 Some experimental notes about the CQD's

The carbon quantum dots were loaded on to 65 mg of B8.Rh and submitted for drying at 60 [°C]. During the drying process the solution coagulated, can be seen in picture E.4

From figure E.4 (a) a white area is starting to show, upon reaching dryness the whole solution had coagulated and looked like a white gel. It was decided to dissolve the coagulated solution directly in the photoreactor, and test the photocatalytic activity. During the activity testing, it was observed that the solution was becoming more transparent and that it no longer absorbed all the light. Figure E.4 (b) shows the solution after 24 hour radiation.

(a) The picture shows the how the CQD solution, with 65 [mg] of B8.Rh dispersed, is coagulating during the drying process

(b) Shows the solution of the first experiment with CQD's after 24 [hour] of irradiation with the solar simulator

Figure E.4: (a) Shows the drying process after dispersing B8.Rh in the CQD solution and (b) shows the CQD's solution after 4 [hour] irradiation

The addition of the solution containing the CQD caused the photocatalytic powder to cluster during the photoreaction. It is suspected that this was caused by a polymer, used in the precursor solution for the CQD's and that it is the polymer that is causing

the coagulating during the drying process after wet impregnation. Because of the suspicion toward the polymer, an attempt to remove it by dialysis against deionized water. After the dialysis, 65 mg of B8.Rh was again impregnated with the CQD's. The solution was dried at 60 °C for 48 hours. After being dried the powder appeared to be the only remaining substance.

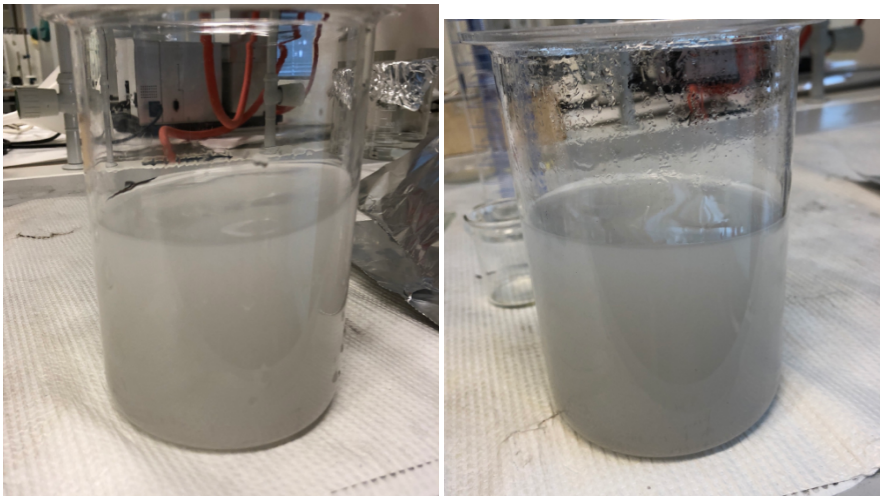

(a) The picture shows the how the solution containing the 65 mg of B8.Rh, impregnated with CQD's dispersed in the second try

(b) Shows the solution of the second experiment with CQD's after 24 [hour] of irradiation with the solar simulator

Figure E.5: (a) Shows the drying process after dispersing B8.Rh in the CQD solution and (b) shows the CQD's solution after 4 [hour] irradiation

Appendix F

GC measurement

Included is a GC-report, from which the H_2 evolution is calculated from, in the activity measurements. During a photocatalytic activity measurement, a report like this is generated every 15. minute and from the report the vol % of H_2 is found and converted into μmoles.

$$\frac{[H_2][\mu mol]}{[mol]of gaseous mixture} \times \frac{[mol]}{22414[ml]} \times \frac{100[ml]}{1[min]} \times 15[min] = H_2[\mu mol] \qquad \text{(F.1)}$$

Agilent Cerity QA/QC Report

Sample name:	SrTiO3.Rh Batch 8 Photo Pt EtOH Destilled water sectry min1215
Sample note:	
Submission time:	Saturday, May 26, 2018 8:16:20 PM
Operator:	
Injection date:	Sunday, May 27, 2018 4:47:58 PM
GC Description:	uGC - SN: US10413005
Signal description:	TCD1 A; TCD2 A
Method:	My standard procedure
Method last saved:	Monday, October 30, 2017 11:00:24 AM

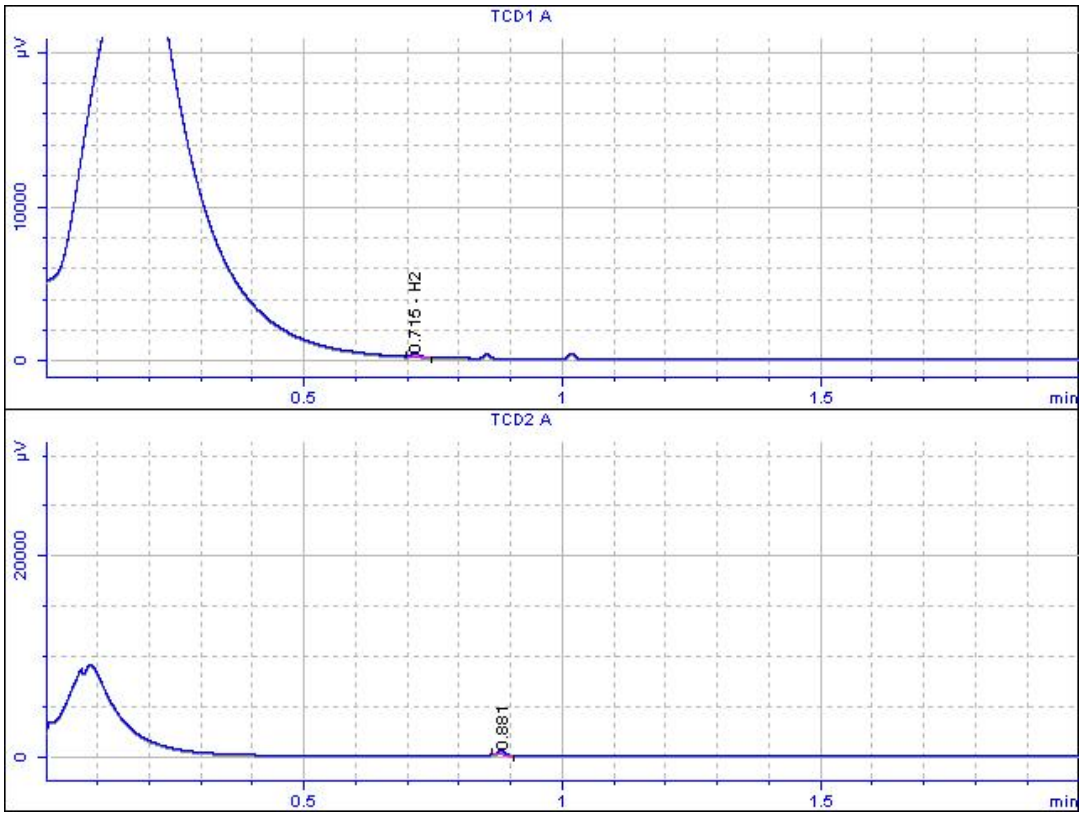

Area Percent Report

Calibration last saved:	Tuesday, October 24, 2017 4:57:24 PM
Multiplier:	1.0000
Dilution:	1.0000
Sample amount:	0.0000 volume%
Sample type:	Sample
Sampling source:	Inlet

Signal	Retention Time [min]	Type	Width [min]	Area [µV*s]	Area %	Name
1	0.715	PP	0.014	234.62505	32.96550	H2
2	0.881	BP	0.011	477.10403	67.03450	

Total Area = 711.729

Report summary:
Warning(s): Sample amount is zero. Absolute amounts calculated

Instrument run log:

External Standard Report (Sample Amount is 0!)

Calibration last saved:	Tuesday, October 24, 2017 4:57:24 PM
Multiplier:	1.0000
Dilution:	1.0000
Sample amount:	0.0000 volume%
Sample type:	Sample
Sampling source:	Inlet

Signal	Retention Time [min]	Type	Area [µV*s]	Amt/Area	Amount [volume%]	Name
1	0.715	PP	234.62505	0.00010	0.02400	H2

```
Total amount = 0.02400
```

Report summary:
Could not generate Percent ESTD Report - sample amount is 0.

Warning(s): Sample amount is zero. Absolute amounts calculated

Instrument run log:

ESTD Report

Calibration last saved:	Tuesday, October 24, 2017 4:57:24 PM
Multiplier:	1.0000
Dilution:	1.0000
Sample amount:	0.0000 volume%
Sample type:	Sample
Sampling source:	Inlet

Signal	Retention Time [min]	Type	Area [µV*s]	Amt/Area	Amount [volume%]	Name
1	0.715	PP	234.62505	0.00010	0.02400	H2

```
Total amount = 0.02400
```

Report summary:
Warning(s): Sample amount is zero. Absolute amounts calculated

Instrument run log:

Norm Percent Report

Calibration last saved:	Tuesday, October 24, 2017 4:57:24 PM
Multiplier:	1.0000
Dilution:	1.0000
Sample amount:	0.0000 volume%
Sample type:	Sample
Sampling source:	Inlet

Signal	Retention Time [min]	Type	Area [µV*s]	Amt/Area	Norm %	Name
1	0.715	PP	234.62505	0.00010	100.000000	H2

Total percent = 100%

Report summary:
Warning(s): Sample amount is zero. Absolute amounts calculated

Instrument run log: